JOURNAL OF GEOPHYSICAL RESEARCH, VOL. 98, NO. D5, PAGES 8611–8638, MAY 20, 1993

Gravity Waves Generated by a Tropical Cyclone During the STEP Tropical Field Program: A Case Study

L. PFISTER,[1] K. R. CHAN,[1] T. P. BUI,[1] S. BOWEN,[2] M. LEGG,[3]
B. GARY,[4] K. KELLY,[5] M. PROFFITT,[5] AND W. STARR[6]

Overflights of a tropical cyclone during the Australian winter monsoon field experiment of the Stratosphere-Troposphere Exchange Project (STEP) show the presence of two mesoscale phenomena: a vertically propagating gravity wave with a horizontal wavelength of about 110 km and a feature with a horizontal scale comparable to that of the cyclone's entire cloud shield (wavelength of 250 km or greater). The larger feature is fairly steady, though its physical interpretation is ambiguous. The 110-km gravity wave is transient, having maximum amplitude early in the flight and decreasing in amplitude thereafter. Its scale is comparable to that of 100-to 150-km-diameter cells of low satellite brightness temperatures within the overall cyclone cloud shield; these cells have lifetimes of 4.5 to 6 hours. Aircraft flights through the anvil show that these cells correspond to regions of enhanced convection, higher cloud altitude, and upwardly displaced potential temperature surfaces. A three-dimensional transient linear gravity wave simulation shows that the temporal and spatial distribution of meteorological variables associated with the 110-km gravity wave can be simulated by a slowly moving transient forcing at the anvil top having an amplitude of 400-600 m, a lifetime of 4.5-6 hours and a size comparable to the cells of low brightness temperature. The forcing amplitudes indicate that the zonal drag due to breaking mesoscale transient convective gravity waves is definitely important to the westerly phase of the stratopause semiannual oscillation and possibly important to the easterly phase of the quasi-biennial oscillation. There is strong evidence that some of the mesoscale gravity waves break below 20 km as well. The effect of this wave breaking on the diabatic circulation below 20 km may be comparable to that of above-cloud diabatic cooling.

1. Introduction

Recent theoretical and observational studies of the tropical stratosphere have shown that synoptic scale and mesoscale inertia-gravity waves are an important contributor to the wave driving of the general stratospheric circulation. Their importance is most clearly established in the upper tropical stratosphere. For example, general circulation modeling studies by *Hamilton and Mahlman* [1988] show that much of the westerly acceleration in the upper stratosphere (~ 45 km) semiannual oscillation (SAO) in their model is due to synoptic scale waves (wavelengths of 1000 to 3000 km) with periods less than 1 day. Moreover, there is evidence that still shorter time and spatial scales may be important. *Miyahara et al.* [1986] found that the momentum fluxes calculated by the GFDL SKYHI general circulation model increased substantially when horizontal grid distances were reduced and that much of this increase was attributable to shorter scale waves. Observational studies also indicate the potential importance of mesoscale phenomena. For example, overflights of convective systems during the 1980 NASA Panama experiment indicate that mesoscale (~110 km) disturbances of significant amplitude are associated with the convection. *Pfister et al.* [1993] (hereafter *P1*) showed that if these disturbances are assumed to be vertically propagating gravity waves, their impact on the upper stratosphere SAO is comparable to that of the planetary Kelvin wave examined by *Hitchman and Leovy* [1988].

Gravity waves may also be important in the tropical lower stratosphere. This region is crucial to stratospheric chemistry because all tropospheric pollutants must pass through it to reach the photochemically active upper stratosphere. The Micronesia region in January is particularly important in this regard, since the extreme dryness of the lower stratosphere suggests that a disproportionate amount of tropospheric air passes through this particularly cold portion of the tropical lower stratosphere [*Newell and Gould-Stewart*, 1981]. Deep convection provides a continuous pumping action to the lower stratosphere through rapid changes in the altitude of the tropopause on scales from 5 to 200 km. These changes in tropopause altitude can be quite large, about 1-2 km for mid-latitude severe convective storms [*Heymsfield and Blackmer*, 1988], somewhat less for tropical systems [*P1*]. The altitude changes are likely to excite gravity waves, which can easily propagate through the highly stable stratosphere. If these gravity waves encounter either critical levels or levels of weak winds, they may break. As in the upper stratosphere, the resulting dissipation of the gravity wave will exert a drag at the level of wave breaking, with consequences for the lower stratospheric momentum budget.

How important these convectively excited mesoscale gravity waves are to the momentum budgets of either the lower or the upper stratosphere depends on evaluating their amplitudes and characteristic length and time scales. Previous work using fast response aircraft measurements of pressure and temperature [*Pfister et al.*, 1986, 1993] showed that characteristic peak-to-peak deviations in the altitude of constant θ surfaces are 300-400 m for disturbances on the scale of tropical anvils (~100 km) and perhaps twice that for

[1]NASA Ames Research Center, Moffett Field, California
[2]San Jose State University, San Jose, California.
[3]Synernet, Fremont, California.
[4]Jet Propulsion Laboratory, Pasadena, California.
[5]NOAA Aeronomy Laboratory, Boulder, Colorado.
[6]Los Altos Hills, California.

Paper number 92JD01679.
0148-0227/93/92JD-01679$05.00

disturbances on the scale of convective turrets (~5 km). However, because of the "snapshot" nature of aircraft measurements, time scales (and hence phase speeds) could not be measured but had to be derived indirectly from satellite imagery. Implicit in this procedure are the two assumptions that the observed temperature disturbances are (1) part of a gravity wave field and not associated with some other dynamical phenomenon and (2) directly caused by the underlying convection. Data from the January 1987 Darwin, Australia, field mission of the Stratosphere-Troposphere Exchange Project (hereafter STEP tropical) that includes not only temperature at the aircraft altitude but also aircraft winds and vertical temperature profiles along the aircraft flight path are well suited to experimentally verifying these assumptions.

This case study addresses four basic scientific questions relating to convectively generated stratospheric mesoscale gravity waves. First, can we clearly show that the observed mesoscale temperature variations in the lower stratosphere are indeed gravity waves? Second, can we unambiguously establish a source or sources for these gravity waves? Third, what are the actual mechanisms by which deep convection generates mesoscale stratospheric gravity waves? And finally, what is the impact of these gravity waves, both on the lower stratosphere over Micronesia during STEP and on the middle and upper stratosphere? To address these four questions, we will do a case study of a gravity wave excited by a tropical cyclone, including mechanistic gravity wave modeling. We will present data from the lowest 2 km of the stratosphere above a tropical cyclone and from the cloud tops of the cyclone itself in section 2. These data will show the presence of mesoscale gravity waves in the lower stratosphere and suggest the generation mechanism at the cloud tops. Sections 3 and 4 show the results of steady state and transient simulations of the gravity wave, respectively, using the forcing mechanisms suggested by aircraft and satellite measurements. The last two sections will summarize the results and discuss the potential effects of the gravity waves on the stratospheric circulation.

The available data and instruments on the ER-2 aircraft are discussed in some detail by *Russell et al.* [this issue]. Of special importance to this study are the measurements of meteorological variables, including horizontal wind, vertical wind, pressure, and temperature made by the meteorological measurement system (MMS) [*Chan et al.*, 1989], and vertical temperature structure made by the microwave temperature profiler (MTP) [*Gary*, 1989]. By its very nature the distribution of aircraft measurements is very anisentropic in both space and time, so auxiliary synoptic scale data are essential for the interpretation of aircraft data. The most important data set was the 3 hourly infrared imagery from the Japanese geosynchronous weather satellite (GMS) produced for the International Satellite Cloud Climatology Project (ISCCP) archive. These images have the advantage of providing satellite brightness temperature (T_{sat}) resolution below the 199 K cutoff of the routine IR images, which is of special importance when cloud top temperatures are between 183 K and 193 K. Special radiosonde ascents from the Australian Monsoon Experiment (AMEX) were also useful in the study.

2. Observations of Cyclone Jason

Cyclone Jason (Figure 1) developed late on February 6, 1987, near the center of the Gulf of Carpentaria. It moved slowly westward at an average speed of ~2 ms^{-1} for its first 48 hours, a period which included STEP tropical flight 12, which took place between approximately 0100 and 0500 UT on February 8. This westward motion was not constant, however; as Figure 1 shows, between 2100 UT (February 7) and 0300 UT (February 8) the main cloud shield of the cyclone (as defined by $T_{sat} < 223$ K) was essentially stationary.

The intensity of the cyclone as measured by the area of $T_{sat} < 186$ K also varied, as is clear from the sequence in Figure 1. Seven hours before the flight at 1800 UT, there is a large area of $T_{sat} < 186$ K centered just west of the southern end of the ER-2 flight pattern, with a north-northwestward extension of $T_{sat} < 191$ K. Three hours later the area of $T_{sat} < 186$ K has shrunk substantially and moved slightly northeastward, while the convection in the north-northwestward extension has intensified, resulting in the appearance there of temperatures less than 186 K. By 0000 UT on February 8 the northwestward extension has essentially disappeared; the main center of low T_{sat} at the southern end of the flight pattern, however, has enlarged somewhat. After 0000 UT the area of $T_{sat} < 186$ K moves southwestward and diminishes, with some slight revival of convective activity to the northwest.

Flight 12 began at Darwin at about 0100 UT on February 8. The aircraft proceeded due east at 18.3 km, about 2 km above the tropopause (see Figure 2). The aircraft turned near 135°E, headed southwestward, and descended just east of the cyclone's cirrus shield. After a short flight leg within the cirrus anvil at 16.4 km, the aircraft ascended to 16.75 km to avoid severe turbulence, turning northward shortly thereafter. Moderate turbulence continued for another ~140 km while the aircraft was within or just above the cirrus anvil. North of 12.3°S, the approximate latitude of the initial 18.3 km overflight, the cloud top altitudes were lower and there was no turbulence. After flying southeastward near the northeastern edge of the cloud shield, the aircraft ascended to 17.1 km and began a series of three east-west flight legs across the northern portion of the cloud shield. After turning eastward and ascending to 17.65 km at the western end of the first flight leg, the inertial navigation system (INS) failed; the position of the aircraft on the remaining two legs at 17.65 km (eastward) and 18.3 km (westward) has been approximated by dead reckoning for a portion of this study but is not shown in Figure 2 or Figure 1.

2.1. *Stratospheric Aircraft Observations*

Figure 3 shows time series for the initial 18.3 km overflight of the cyclone between 0200 and 0230 UT (leg 1, solid line in Figure 2). Plotted in Figure 3 are the meteorological variables [*Chan et al.*, 1989; *Gary*, 1989] and the underlying IR brightness temperature from the 0300 UT (February 8) GMS IR image. With the exception of the underlying GMS brightness (which has a resolution of 10 km) these data have been filtered to remove fluctuations with horizontal wavelengths less than 15 km. This filtering scheme is used for all aircraft data shown unless otherwise noted. At about 137.5°E the measured temperature begins to rise, reaching a peak ~5 K above background at 138.2°E and falling back by about 138.7°E. The "wavelength" of the phenomenon is about 1° of longitude, or ~110 km; it is comparable in size to the dip below 205 K satellite brightness temperatures. The two horizontal wind components are also varying in this region and are somewhat correlated with each other; however, the most important observation here is that the meridional wind variation associated with this ~110-km phenomenon is small compared to the zonal wind

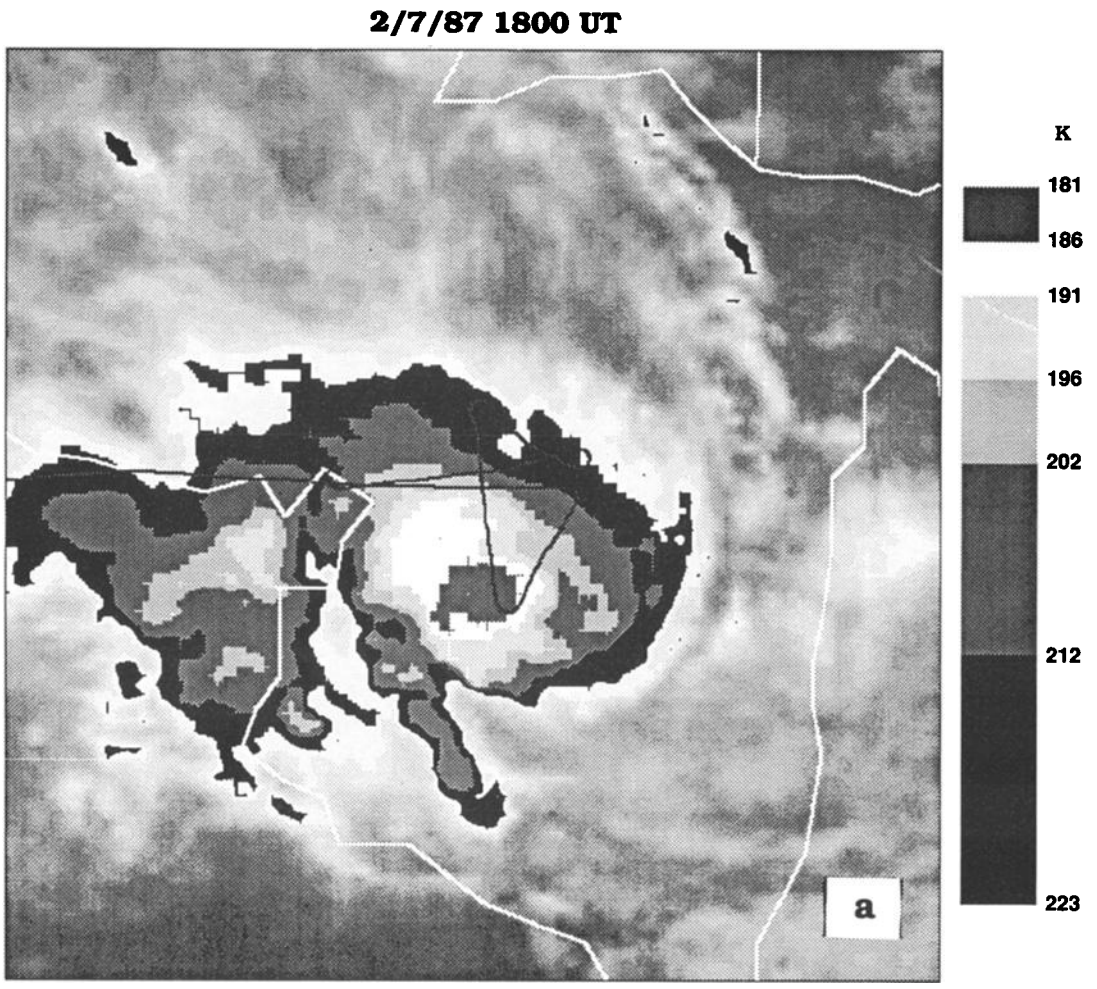

Fig. 1. (*a*)-(*e*) Sequence of 3 hourly geosynchronous weather satellite (GMS) IR images of Cyclone Jason from 1800 UT on February 7, 1987, through 0600 UT on February 8, 1987. The ER-2 flight track over the cyclone is shown on each image. For the 0300 UT image on February 8, aircraft winds at 16.75 km and 100-mbar (~16.5 km) radiosonde winds at Weipa are shown.

variation. Another key observation is that the zonal wind (u) maximum does not coincide with the temperature (T) peak; instead, it is the horizontal gradient of the zonal wind that is in phase with the temperature maximum. Conversely, the extrema in u coincide with the east-west gradients in T. This quarter-cycle phase relationship between the wind and the temperature fields is the hallmark of gravity wave motions [*e.g. Holton*, 1979, p.163].

The bottom box of Figure 3 shows the contours of the potential temperature θ in the east-west vertical plane. The pronounced peak in the in situ temperature displayed in the top box of the figure manifests itself as an ~1° of longitude wide dip in the theta contours just east of 138°E at the aircraft altitude, with a pronounced rise in those contours to the west. The upward and eastward slope of the location of the dip is clear from 17 to 19 km and is another hallmark of gravity wave motion [*e.g. Holton*, 1979, p. 163]. The maximum peak-to-peak displacement of the θ surfaces of about 300 m occurs near the aircraft flight altitude, decreasing somewhat both above and below. Such displacements are comparable to values observed in the stratosphere for these horizontal scales over deep convection in other tropical locations [*P I*]. However, they are substantially smaller than the 1-to 2-km vertical displacements induced by topography [*Gary*, 1989].

Quantitative as well as qualitative agreement with gravity wave theory is apparent in these observations. In a slowly varying basic state, assuming a two-dimensional, nondissipative, linear gravity wave with perturbation quantities χ' expressed as

$$\chi' = \mathrm{Re}\left(\chi_0 e^{i(kx+\lambda z-\omega t)} \right) \tag{1}$$

the dispersion relationship is

$$\frac{k}{\lambda} = \frac{\pm\hat{\omega}}{\omega_b} \tag{2}$$

with

$$\hat{\omega} = \omega - k\bar{u}$$

ω_b = Brunt – Vaisala frequency = $2.4 \times 10^{-2} s^{-1}$

$\bar{u}$ = basic state zonal wind = $-8\ ms^{-1}$

$k = 5.7 \times 10^{-5}\ m^{-1}$

The perturbation amplitudes u, w (vertical wind), T, and T_z are then related by

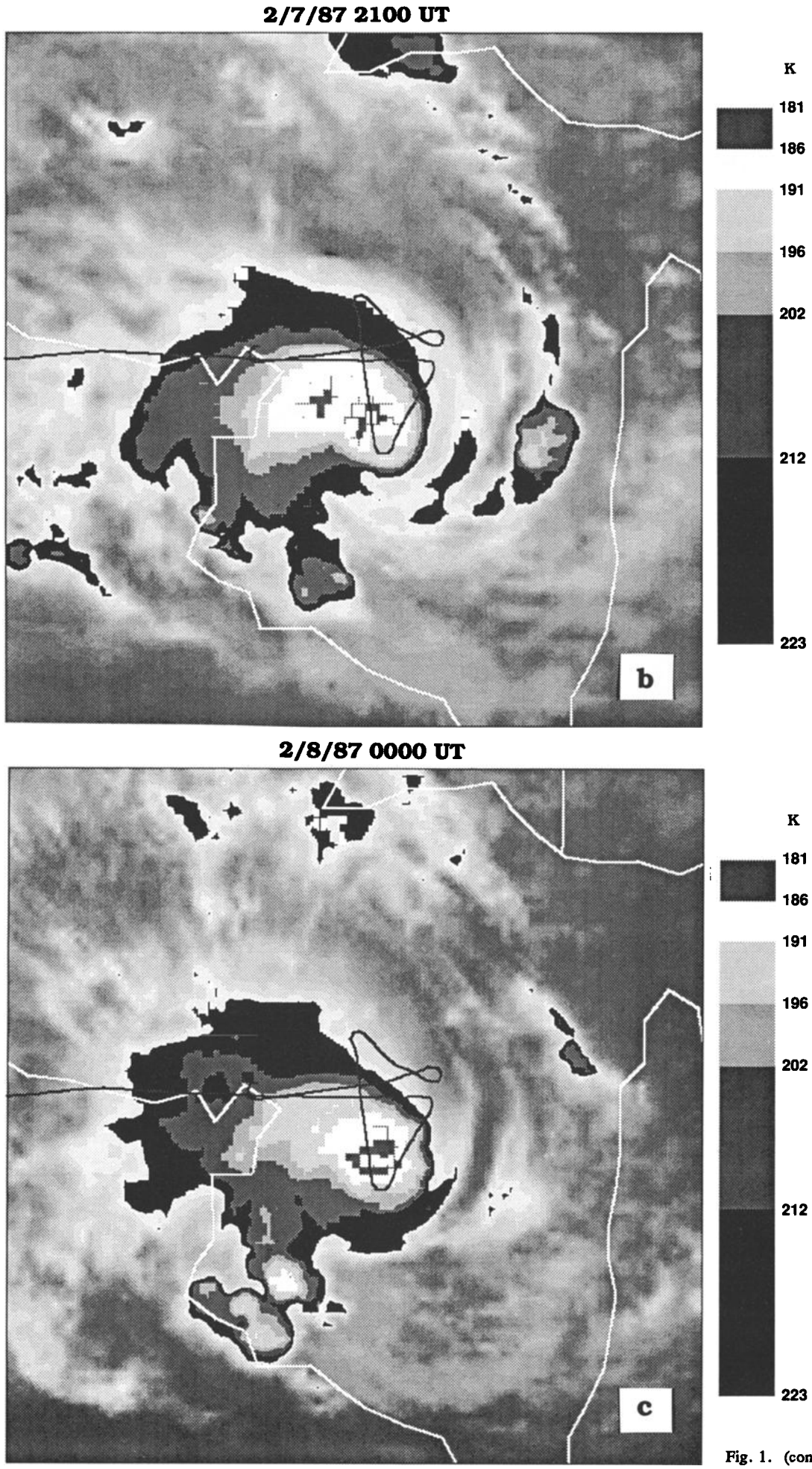

Fig. 1. (continued)

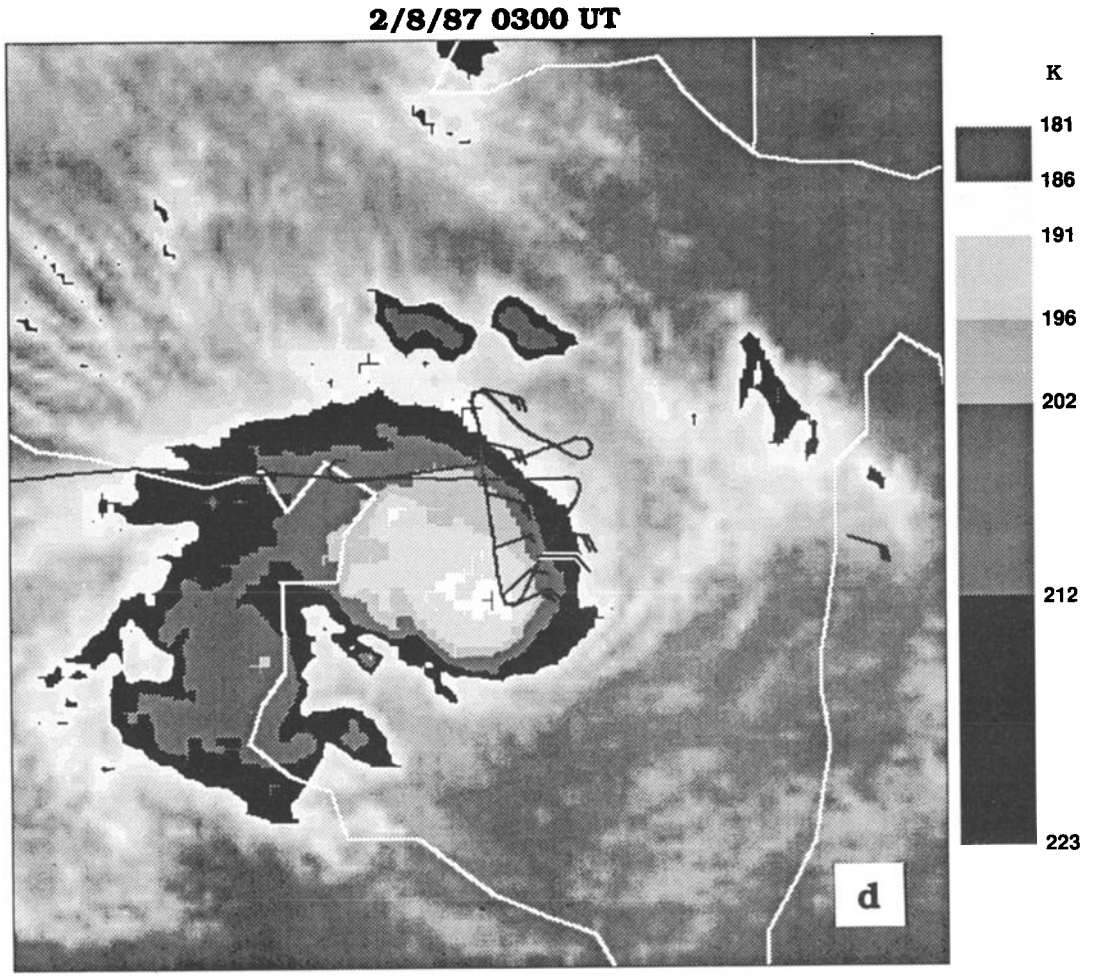

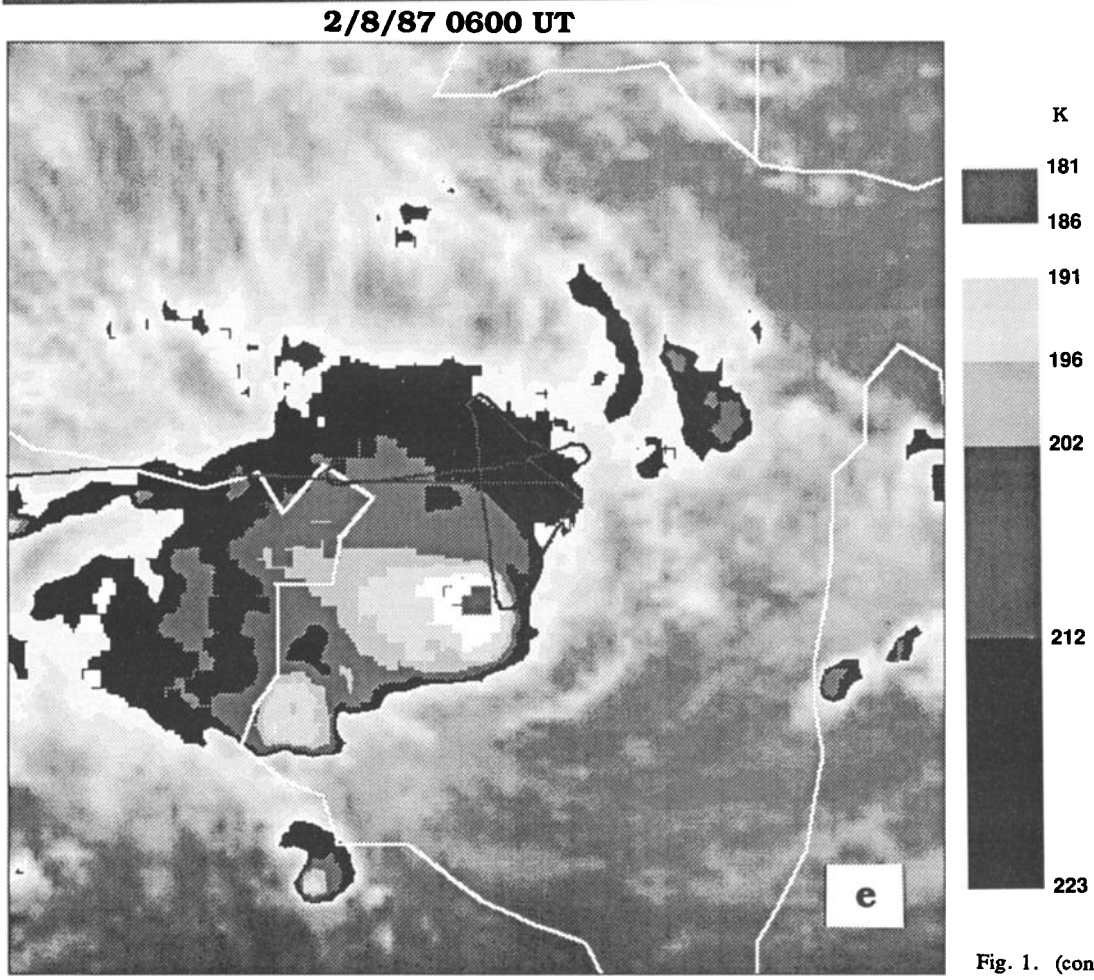

Fig. 1. (continued)

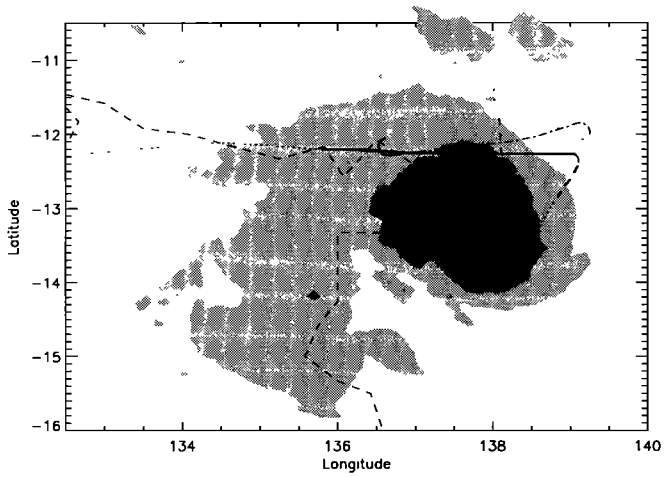

Fig. 2. GMS IR image for 0300 UT on February 8, 1987, with flight track of the ER-2 superimposed. Light shading, IR brightness temperatures between 202 and 223 K; medium shading, brightness temperatures between 191 and 202 K; dark shading, brightness temperatures less than 191 K. The following sections are highlighted and referred to in the text: leg 1 (solid line), initial 18.3-km flight over the cyclone; descent *a* (heavy dashed line), descent east of the cyclone; leg 2 (dashed line), anvil pass at 16.75km; leg 3 (dashed-dotted line), 17.1-km flight leg just above the anvil; ascent *b* (heavy solid line), ascent on west side of the cyclone.

$$w = \frac{i\hat{\omega}R}{H\omega_b^2}T \tag{3}$$

$$u = \frac{\mp iR}{\omega_b H}T \tag{4}$$

$$T_z = i\lambda T \tag{5}$$

R = gas constant = 287 m^2s^{-2} K^{-1}

H = atmospheric scale height = 6.34 km

There are no obvious gravity wave sources above the level of observation, so the energy flux is almost certainly upward, implying a choice of the negative sign in (2) and the plus sign in (4). This, in turn, implies two things: first, that the zonal wind peak appears to the west of the temperature peak (as is observed in Figure 3), and second, a particular ratio of magnitudes of the zonal wind and temperature perturbations that is independent of the vertical wavenumber λ. Using (4) and the observed peak-to-peak T of 5 K, we calculate a peak-to-peak u of 9.4 ms^{-1}, very close to the observed value of 8.8 ms^{-1}.

The temperature-horizontal wind relationship is independent of wave frequency and vertical wavenumber. The fact that it is satisfied is a quantitative indication that the phenomenon is a gravity wave. However, the observations also contain vertical wavenumber information which suggests a source for the wave energy. Since the temperature peak is a quarter cycle to the west of the vertical temperature gradient peak, (5) then implies that the vertical wavenumber is negative (upward and eastward slope of the phase surfaces), with a value of about -2.5 km^{-1}. From (2) the Doppler-shifted frequency $\hat{\omega}$ is positive with a value of $\hat{\omega}$=5.5x$10^{-4}s^{-1}$. This is quite close to the stationary wave value of 4.6x$10^{-4}s^{-1}$. Thus to zeroth order, the observed 110-km wave is quasi-stationary, presumably excited by tropopause level flow over a particularly cold (and presumably high) portion of the cyclone's cloud shield.

From (3) the peak-to-peak w = 0.21 ms^{-1}. This is comparable to the claimed ER-2 MMS vertical wind precision of ± 0.1 ms^{-1} [*Scott et al.*, 1990] so one would not expect the measured vertical winds associated with this phenomenon to have good quantitative agreement with this estimate. Indeed, though the low-pass filtered vertical winds (not shown) are qualitatively in agreement with (3), the peak-to-peak variation is more than a factor of 2 larger, with substantial sensitivity to the specific filter used.

Another notable feature of the theta surface displacements is that the amplitude of the ~1° wide dip decays rapidly above and below 18 km, becoming almost negligible below 17 km. Below 17 km the theta surface variation is dominated by a large-scale upward and eastward slope. This larger scale of variation is also apparent at 18.3 km, as shown in Figure 4, which depicts the entire initial 18.3-km flight leg (leg 1 plus the dotted line section to the west in Figure 2). This figure illustrates variations on the scale of the cloud shield as a whole. The gravity wave at 138°E can be seen as a substantial perturbation on a larger-scale correlated variation of zonal wind and temperature. Near 135.5°E the zonal easterlies, the temperature, and the vertical temperature gradient all begin to decrease. Since the temperature and wind variations are in phase, this is clearly not a linear gravity wave phenomenon.

Figure 5 shows the meteorological variables from the second longitudinal pass over the cyclone's cloud shield (leg 3, the dashed-dotted line in Figure 2 at 17.1 km). This pass occurred at about 0330 on February 8, about 1 $\frac{1}{4}$ hours after the gravity wave observation in Figure 3. As shown in Figure 2, the horizontal location of this flight leg was very close to the initial leg 1; thus a comparison of the theta contours to Figure 3 should yield some insight into the temporal behavior of the temperature above the cyclone. The differences at 18.3 km (the leg 1 flight level) are significant. The longitudinal position of the 110-km "wavelength" dip is now at 137.8°E instead of 138.2°E, but the most important feature is the smaller amplitude, about 100-200 m of theta surface vertical displacement. Below 17.5 km, near the leg 3 flight level, there is more consistency between Figure 3 and Figure 5; as in Figure 3, the variance is dominated by an undulation extending over the entire cloud shield of the cyclone. (There is also evidence of the shorter-scale temperature peak just west of 138°E.) One important difference from the leg 1 observations is that the large-scale undulation displays classic gravity wave characteristics, namely, the quarter cycle phase relationship between the temperature and the horizontal wind perturbations. This is apparent from the location of the temperature minimum for the flight leg at 138.5°E, halfway between the extrema of zonal wind. Another example of a cyclone-scale gravity wave is documented in *Danielsen* [this issue]. It is notable that the downward and downstream slope of the potential temperature surfaces is qualitatively similar to that observed above the tops of severe convective storms [*Johnson et al.*, 1990].

Figure 6 and Figure 7 show the meteorological variables as the aircraft traverses the cyclone from west to east at 17.6 km (about 0355 UT) and east to west at 18.3 km (about 0420 UT) respectively. As indicated above, the INS failed at 0345 UT, so no wind or horizontal position data are available. The longitudes in the two figures are based on the pilot's log (stating that he was flying eastward) and dead reckoning (based on true airspeed and estimates of the winds). The longitudes are thus highly uncertain, especially for Figure 7, since it is not known when the aircraft turned at the end of the 17.6-km leg.

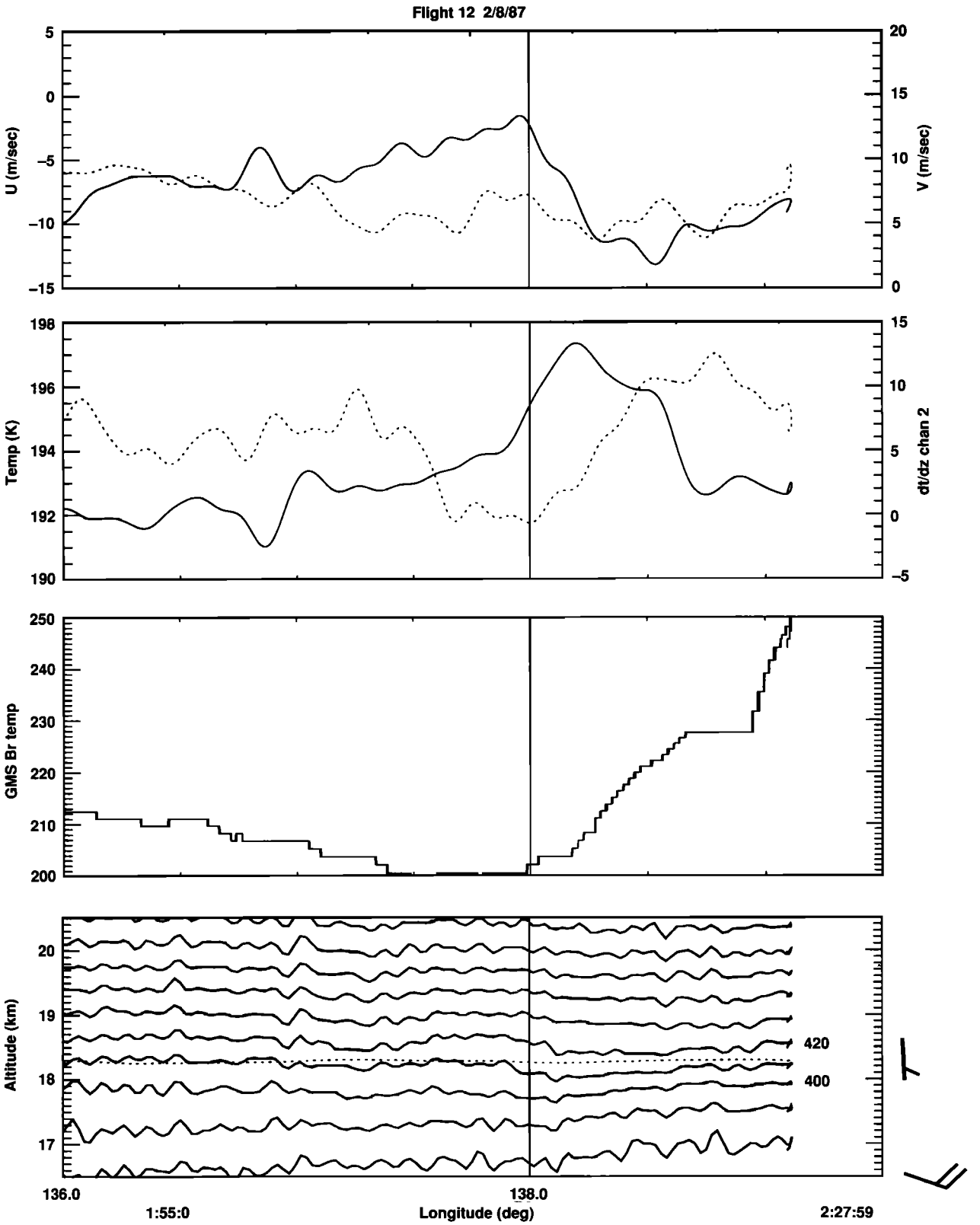

Fig. 3. Meteorological variables as a function of longitude for the initial 18.3-km overflight of Cyclone Jason (leg 1 in Figure 2). (Top box) Zonal wind u (solid line) and meridional wind v (dotted line) from the ER-2 meteorological measurement system (MMS) [*Chan et al.*, 1989]; (second box) temperature T (solid line, from ER-2 (MMS) and vertical temperature gradient [dotted line, from channel 2 of the ER-2 microwave temperature profiler (MTP), *Gary et al.*, [1989]; (third box) brightness temperatures from the 11.5- μm channel of the 0300 UT GMS image underlying the aircraft flight path; (bottom box) contours of potential temperature at 10° intervals within a 4-km deep swath above and below the aircraft altitude (solid lines, from the ER-2 MTP) and the aircraft flight altitude (dotted line). Wind barbs to the right of the bottom box are from Weipa, about 275 km east-southeast of the eastern end of leg 1 (see Figure 1*d*).

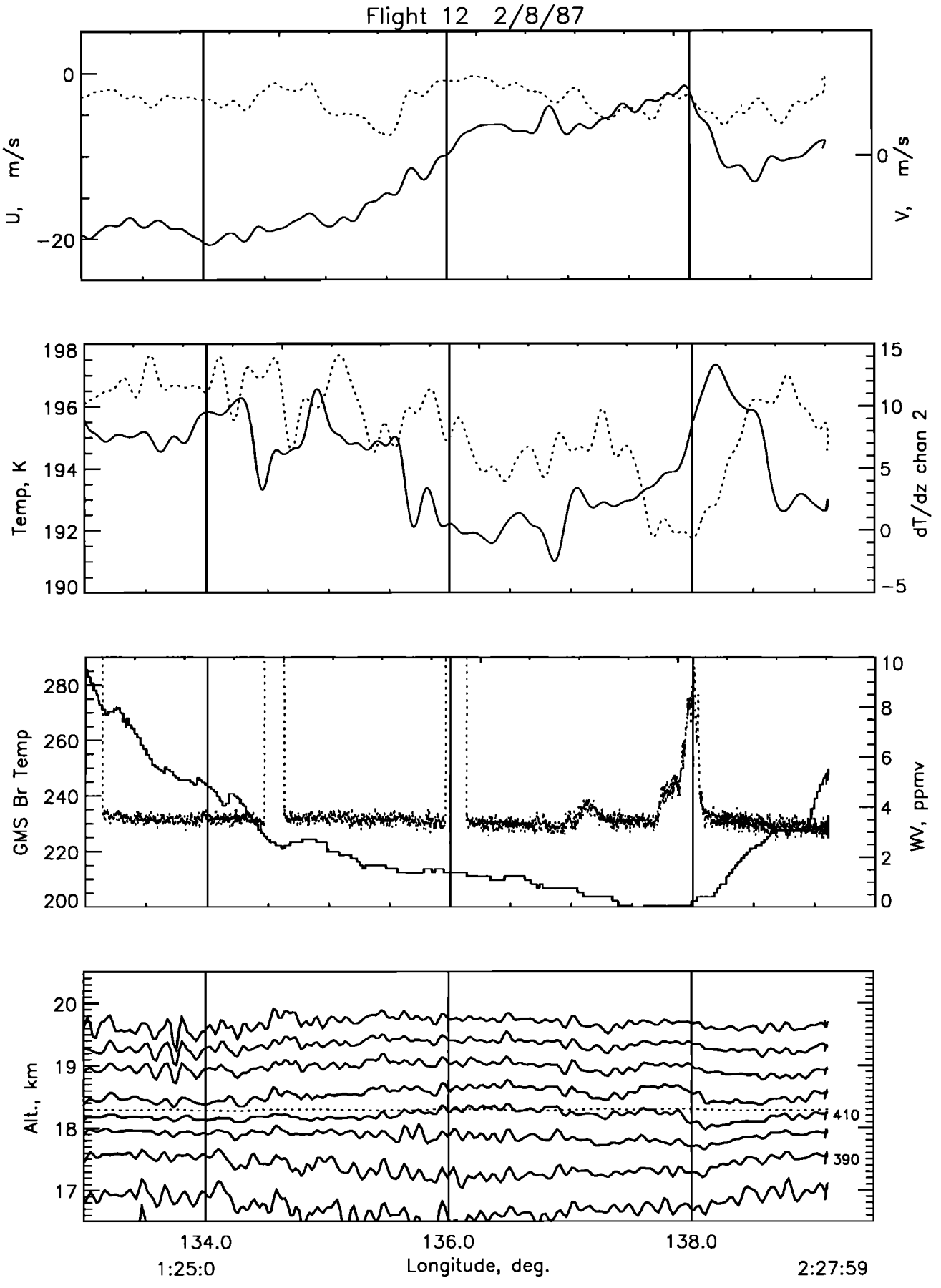

Fig. 4. As in Figure 3 except for the entire initial 18.3-km flight leg from just east of Darwin to the end of leg 1 in Figure 2. The third box now includes the water vapor measurement (dotted line; see *Kelly et al.* [this issue]).

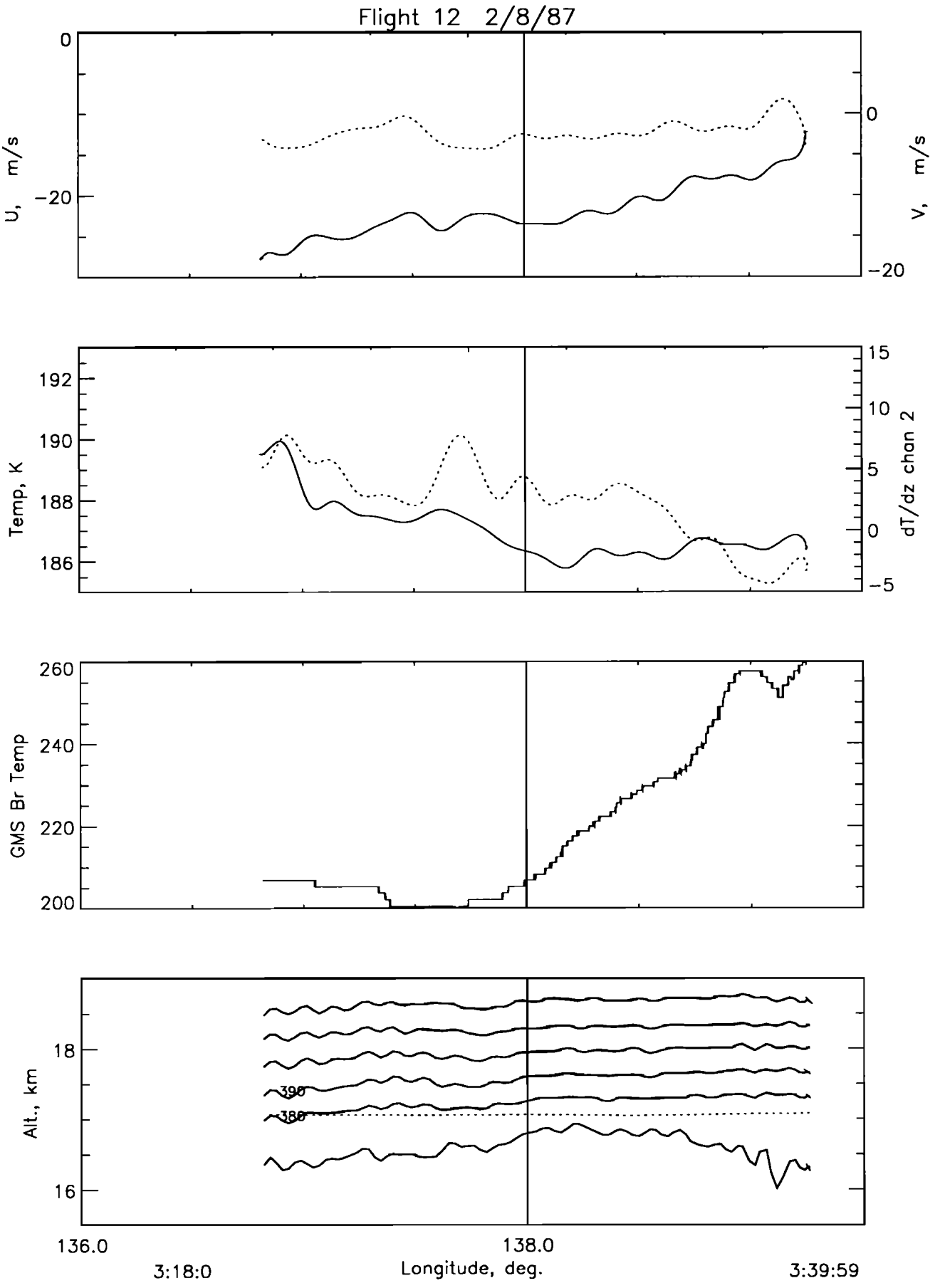

Fig. 5. As in Figure 3, except for leg 3.

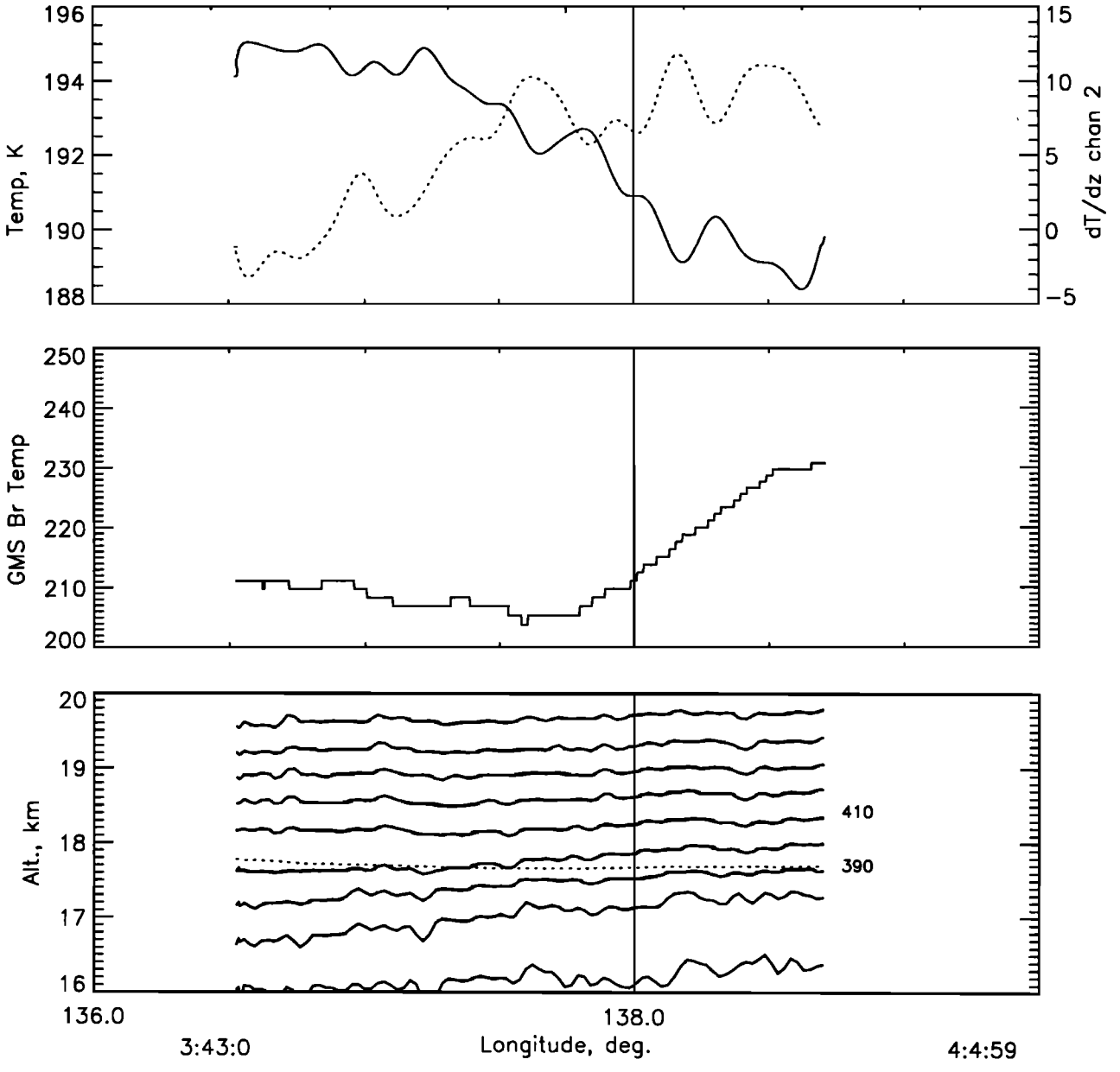

Fig. 6. Meteorological variables as a function of longitude at 17.6 km. (Top box) Temperature T (solid line, from ER-2 MMS) and vertical temperature gradient T_z (dotted line, from channel 2 of ER-2 MTP); (second box) brightness temperatures from the 11.5-μm channel of the 0300 UT GMS image underlying the aircraft flight path; (bottom box) contours of potential temperature at 10° intervals within a 4-km deep swath above and below the aircraft altitude (solid lines, from the ER-2 MTP) and the aircraft flight altitude (dotted line).

Nevertheless, given the last known location of the aircraft, it is likely that both traverses were made at roughly the same latitude as legs 1 and 3.

These two figures are consistent with Figure 5 in that (1) the amplitude of the ~110-km wave disturbance is reduced from the value in leg 1 (Figure 3) and (2) there is clear evidence of the continued presence of the larger-scale phenomenon in the form of a clear upward and eastward slope of the theta surfaces, particularly at the lower altitudes. The data in Figure 7, obtained at the same altitude as that from leg 1, are particularly revealing in that they allow comparison of in situ data at approximately the same location at two different times. What it shows is that the warm bulge at 138.5°E in Figure 3 has moved, broken up, and been reduced in amplitude. The change in the theta contours is also pronounced, with much smaller amplitudes on the ~110-km scale than Figure 3.

2.2. *Anvil Data*

The above discussion has already suggested that the temperature rise at 138.5°E in Figure 3 may be induced by convection, a hypothesis which is certainly reinforced by the placement of the temperature rise near a feature of similar scale in the underlying satellite brightness temperature. Fortunately, this flight included a leg at the cloud level; thus there is an opportunity to examine the convection itself for features having the same scale as the observed gravity wave.

Figure 8 shows the meteorological variables and total water at

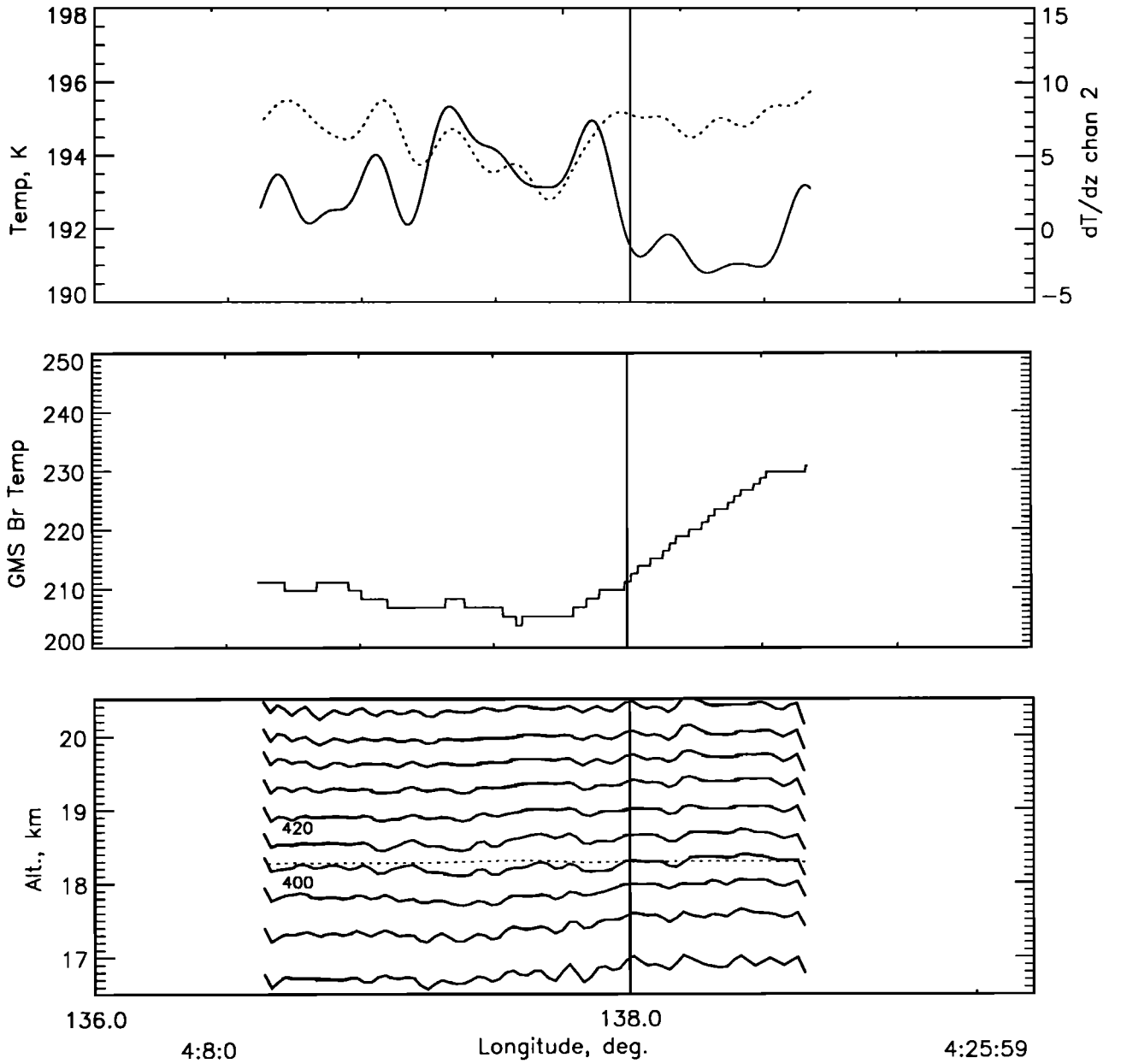

Fig. 7. As in Figure 6, except for the second 18.3-km traverse of the cyclone.

16.75 km (leg 2, the dashed line in Figure 2). Unlike the previous figures the data in this figure are unfiltered. The wind barbs are also plotted in Figure 1*d*. The most obvious features are the substantial enhancements in total water found between 13.5°S and 12.5°S, at which point the aircraft is in and out of a cloud. Notably, the size of this region is comparable to that of the warm peak in Figure 3; moreover, the cloud region corresponds roughly to the region of GMS brightness temperatures less than 191 K in Figure 1*d*. North of this region the cloud is below the aircraft, and the underlying GMS brightness temperatures are correspondingly higher. During the cloud passage the zonal easterly wind is both weaker and substantially more turbulent than outside the cloud. In fact, a section of the flight, 5 min earlier than the one shown, proved sufficiently turbulent to require evasive action by the pilot.

The temperature fluctuations both within and outside the cloudy region are quite small, spanning a range of only 1.5 K if the jump near the northern end is excluded. Nevertheless, the temperature is perceptibly colder within the cloudy region by 0.5–1 K. This is consistent with the potential temperature contours, whose altitudes (particularly the 370° contour, closest to the aircraft flight level) decrease by about 150 m as the aircraft flies northward out of the cloudy region at 12.5°S. As the aircraft approaches the edge of the cloud shield near the northernmost point of the flight, the altitude of the 370° contour drops by another 200 m or so. Below the flight level there is a marked near absence of contours, indicating lapse rates which are close to adiabatic, at least south of 12.5°S. This is also the region where the agreement between the GMS brightness and the in situ temperatures is best. This indicates that the aircraft is flying close to the top of an optically thick cloud. North of 12.5°S the stability is somewhat larger, which is expected since the convective activity and turbulence which tend to produce adiabatic lapse rates are less.

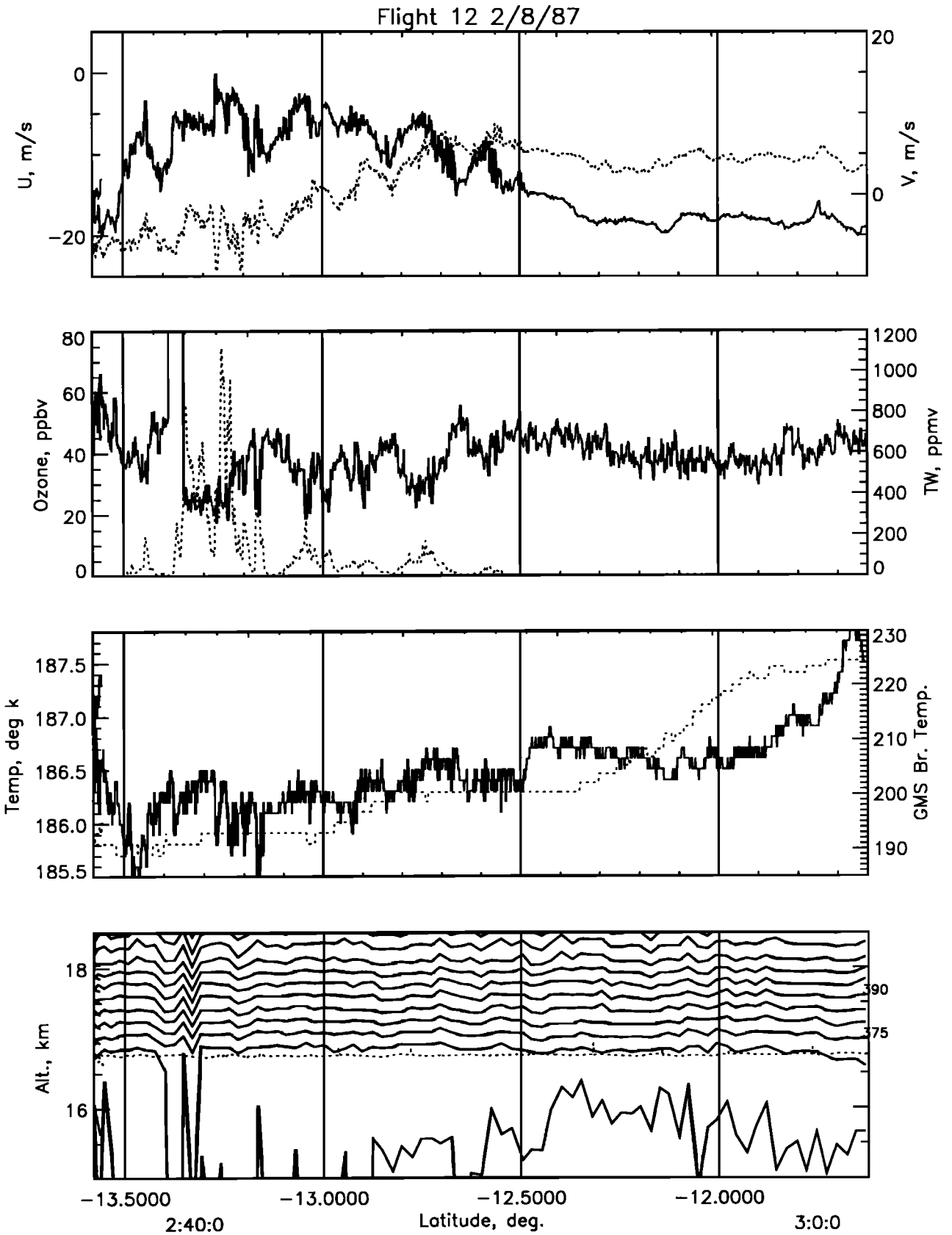

Fig. 8. Meteorological variables and tracers as a function of latitude for the anvil pass through Cyclone Jason (leg 2 in Figure 2). (Top box) Zonal wind u (solid line) and meridional wind v (dotted line) from the ER-2 MMS; (second box) ozone mixing ratio (solid line, *Proffitt et al.*, [1989] and *Starr and Vedder* [1989]) and total water (dotted line, *Kelly et al.*, [this issue]); (third box) temperature T (solid line, from ER-2 MMS) and brightness temperatures from the 11.5-μm channel of the 0300 UT GMS image underlying the aircraft flight path; (bottom box) contours of potential temperature at 5° intervals within a 3.5-km deep swath above and below the aircraft altitude (solid lines, from the ER-2 MTP) and the aircraft flight altitude (dotted line).

The character of the horizontal wind and temperature variations suggest that the coldest portion of the cyclone at 0300 UT depicted in Figure 1*d* is acting as a spongy barrier to the prevailing easterly flow at the flight level. The behavior of both the winds and the temperatures supports this interpretation. The zonal wind decreases markedly from the values prevailing both outside the cloudy region north of 12.5°S and upstream at the Weipa radiosonde station (see Figure 1*d*). The surface air in this case, which given ozone values as low as 20 parts per billion by volume (ppbv) presumably accounts for a significant fraction of the cloud, is not moving westward at 20 ms^{-1}. As strong easterlies impinge on the cloudy air mass, mixing does occur but not enough to accelerate the surface air to speeds anywhere near those of the prevailing easterlies. Instead, the air appears to move around and over the highest and coldest part of the cloud (as manifested by the brightness temperatures in Figure 2). The wind barbs clearly show the divergent motion more or less around the region of brightness temperatures less than 191 K. The higher elevation of the potential temperature contours south of 12.5°S in Figure 8 indicates that the stratospheric air is moving over the bulge in the tropopause created by the region of strong convection.

The elevation of this tropopause bulge is actually quite small, only 150 m, as indicated above. This is substantially smaller than the 300-m dip in the potential temperature contours in Figure 3. As Figure 2 shows, though, the aircraft is moving at the eastern edge of the region of coldest brightness temperatures. It is thus not unreasonable to infer that the actual elevation of the potential temperature surfaces over the coldest part of the cloud might be substantially higher, especially since the time of the 0300 UT image in Figure 2 is within minutes of the actual time of the cloud passage. Figure 5, for example, shows theta surface elevation changes of perhaps 400 m across the cloud shield. Though these observations are well north of the most active convection and have a different horizontal scale, they give an indication of what the effective convectively induced mesoscale upward deviation of the tropopause level might be.

2.3. *Summary of the Observations*

These observations show two mesoscale features in the stratosphere overlying the cyclone and suggest mechanisms that could produce these features. The larger-scale feature, comparable in scale to the cyclone cloud shield as a whole, is quite steady in that it is observed on each flight leg. However, its interpretation is ambiguous. At and below 17.6 km it has the qualitative characteristics of a linear gravity wave; at 18.3 km, though, the characteristic gravity wave quadrature relationship between wind and temperature is replaced by an in-phase relationship.

One explanation for this ambiguity is that there are really two different phenomena. At 17.1 km (Figure 5), flow over a cyclone-uplifted tropopause induces a gravity wave analogous to a mountain wave [see also *Danielsen*, this issue]. At 18.3 km, however, mixing by convection may actually govern the cyclone scale feature. That this may be the case is suggested by the enhancements in the water vapor mixing ratio between 137.5°E and 138°E in Figure 4. The second enhancement is particularly striking; here the mixing ratio approaches 10 ppmv, over twice the prevailing value at these altitudes. Such large mixing ratios imply that some tropospheric air has mixed up to these levels presumably by the overshoot of convective turrets. This is reinforced by the fact that the horizontal wind is almost southerly, coming directly from the region overlying the coldest GMS brightness temperatures in Figure 2 (and presumably the strongest convection). Also suggestive are the correlated sharp increase in meridional wind and sharp decrease in temperature at 135.5°E; it is evidence for colder air mixed in from convection to the south of the flight track being advected to the aircraft's latitude.

That mixing from below is more apparent at 18.3 km than at the lower altitudes seems paradoxical. In fact, though the enhanced water vapor clearly demonstrates convective mixing, there is no proof that its magnitude is sufficient to produce the region of low easterlies, low temperatures, and low vertical temperature gradients east of 135.5°E. Also, the presence of ice crystals during leg 3 [*Knollenberg et al.*, this issue] suggests mixing is occurring there also, with no perceptible effect on the magnitude of the easterlies. One important consideration is the three dimensionality of the cyclone phenomenon. Even well upstream of the cyclone, easterly winds are weaker and southerly winds stronger at 18 km than at lower altitudes (e.g., the radiosonde sounding at Weipa, Figure 3 and Figure 1*d*). Thus the stronger convective activity south of both legs 1 and 3 that is clearly evident in the satellite image Figure 1*d* and in the leg 2 data can exert more influence at 18 km.

An alternative explanation of the cyclone scale feature is that it is indeed the same phenomenon at both altitudes but that nonlinear effects have altered the character of the gravity wave at 18.3 km. Greater nonlinearity at 18.3 km is expected since weaker easterlies imply a much smaller magnitude for the linear advective terms in the linear gravity wave equations. Evidence for nonlinearity is suggested by the winds during ascent *b* at the west end of leg 3 (Figure 2), plotted in Figure 9. Both the zonal (u) and the meridional (v) components of the wind change rapidly with altitude, so rapidly that the Richardson number

$$Ri = \frac{\omega_b^2}{u_z^2 + v_z^2}$$

is less than 0.25 over a depth of 200 m. Whether this shear zone is an amplified nonlinear gravity wave or simply a boundary between two air masses (with the upper air mass being convectively influenced air from the south; see Figure 1*d*) is not clear. Later sections of this paper will show theoretical evidence for the presence of nonlinear gravity waves. Nevertheless, complete interpretation of the cyclone scale phenomenon remains an open question.

The observations also show a smaller-scale feature on the initial (leg 1) 18.3-km flight leg, with a wavelength of about 110 km. This feature clearly shows the characteristics of a linear gravity wave, displaying the quarter cycle phase relationship between the temperature on the one hand and the zonal wind and vertical stability on the other. Another important characteristic of this feature is its confinement both in time and in altitude; it is only found with significant amplitude on the initial overflight of the cyclone, and at that time only within the ~3 km centered at the 18.3-km level. Two hours later the wave is significantly weaker.

In situ aircraft data near the anvil top confirm the nonuniformity of the cyclone's cloud shield on the ~110-km scale apparent in the GMS satellite image. Winds measured within the cloud are substantially weaker than the prevailing easterly jet outside the cloud. This observation and the obvious divergence of wind vectors around the region of highest cloud indicate that the convection is acting as a kind of barrier to the

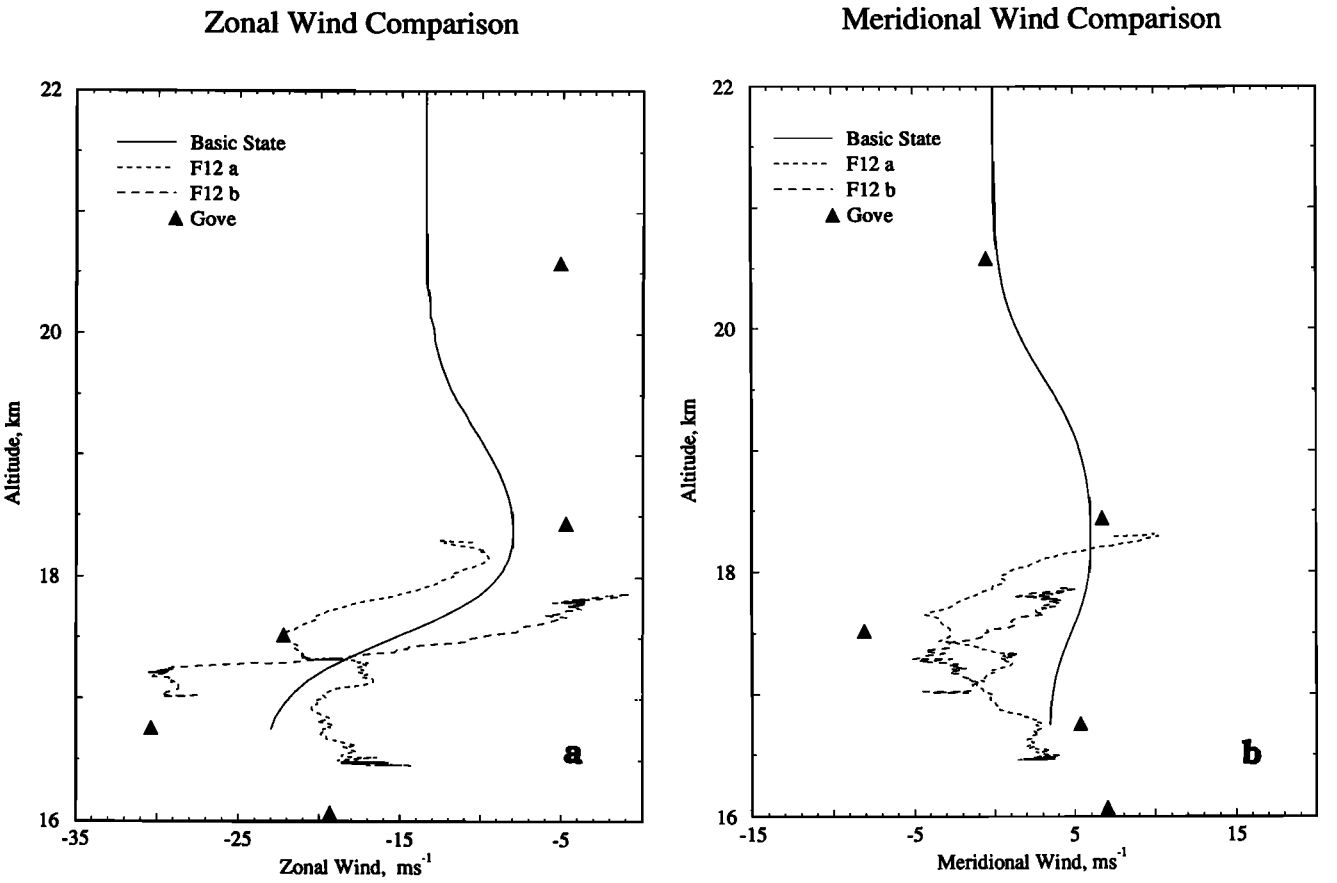

Fig. 9. Altitude dependence of the basic state zonal ($\bar{u}$:(*a*)) and meridional ($\bar{v}$:(*b*)) winds (solid lines). Also shown are vertical profiles from the aircraft at descent *a* (dotted line) and ascent *b* (dashed line) in Figure 2 and winds from Gove (triangles), at the northwest corner of the Gulf of Carpentaria (12.5°S, 136.5°E).

100–mbar easterly jet. Moreover, since the scale of the cloudy region is comparable to that of the 110-km wavelength gravity wave feature, a causal link is indicated. The purpose of the following sections is (1) to establish quantitatively, using gravity wave theory, that this observed feature is indeed a gravity wave and (2) to use linear gravity wave models to establish the nature of the causal link between the variations in the cyclone's cloud field, as revealed by GMS and aircraft measurements, and the observed gravity wave. We will emphasize careful interpretation of the ~110-km feature in these sections for two reasons. First, the length of most of the aircraft legs is too short to allow complete representation of the larger cyclone scale disturbance, and second, though the disturbance is present in some way at all times, it does not display consistent behavior as a gravity wave, particularly on the one aircraft leg which is long enough to properly realize it.

3. Linear Steady State Calculation

The approximate treatment in section 2.1 is at best preliminary, for two reasons. First, it assumes that vertical gradients of the relevant basic state quantities, such as $\bar{u}$, are small (*i. e. Ri* >> 1). In fact, the minimum Richardson number of a reasonable average atmospheric state in the 5 km above the tropopause during the Australian monsoon is of the order of 0.5, largely because of the rapid decrease of the easterly jet with height between ~16 km and ~18 km. Second, this simple treatment tells us very little about either the magnitude or the time variation (if any) of the forcing required to produce the observed disturbance in Figure 3. As shown by *P1*, these are both important parameters in evaluating the potential effects of convective gravity waves on the stratosphere.

Both the GMS images (Figure 2) and the aircraft observations at the anvil top (Figure 8) suggest that the convective disturbance is a localized, crudely elliptical region markedly south of the observations in leg 1. Therefore we expect some horizontal spreading of energy as the gravity wave excited by the isolated region propagates upward from the anvil top at 16.75 km to leg 1 at 18.3 km. Thus a minimum treatment must include variations in both latitude and longitude. We will use a three-dimensional, linear, hydrostatic, steady state treatment in our first attempt to reproduce the observations theoretically. Though the analysis of the data in previous sections indicates that the phenomenon is transient, the results of the steady state case will be useful in understanding what aspects of transience are important.

The paradigm for this first formulation is a steady, horizontally independent flow over two-dimensional (varying in latitude and longitude) topography (see, for example, *Smith* [1980]), except that in this case the "topography" is the variation in tropopause height induced by convection. This mechanism is similar to the "obstacle effect" mechanism for convectively generated gravity waves discussed by *Clark et al.* [1986], except that the horizontal scale is much larger. Instead of individual persistent convective updrafts creating an obstruction to the flow, an ensemble of persistent updrafts

deposits mass into the upper troposphere, raising the isentropes in the lower stratosphere, and causing stratospheric flow around and over the raised isentropes.

If the basic state varies in altitude only, the horizontal dependence in a doubly periodic domain of size L of any perturbation variable $\chi'(x,y,z)$ can be expressed as a two-dimensional (double) Fourier series.

$$\chi'(x,y,z) = \sum_{m=-M}^{M} \sum_{n=-M}^{M} \chi_{mn}(z) e^{2\pi i(mx/L+ny/L)} \tag{6}$$

The horizontal dependence can then be removed from the problem, and after some standard algebraic manipulations we are left with one ordinary differential equation in z for each double Fourier component having x wavenumber $k = 2\pi m/L$ and y wavenumber $l = 2\pi n/L$:

$$\frac{d^2 w_{mn}}{dz^2} + \frac{dw_{mn}}{dz}\left\{\frac{i\alpha_z}{\hat{\omega}} - \frac{1}{H}\right\} + w_{mn}\left\{\frac{k\bar{u}_z + l\bar{v}_z - i\alpha_z}{H\hat{\omega}} + \frac{k\bar{u}_{zz} + l\bar{v}_{zz}}{\hat{\omega}} + \frac{\omega_b^2 \kappa^2}{\hat{\omega}^2}\right\} = 0 \tag{7}$$

Here,

α = Newtonian cooling/Rayleigh friction coefficient

$$w'(x,y,z) = Re\left(we^{i(kx+ly)}\right)$$

$$\hat{\omega} = -k\,\bar{u} - l\bar{v} + i\alpha$$

$$\kappa^2 = k^2 + l^2 \tag{8}$$

$$M = 80$$

$$L = 1.8 \times 10^6 \text{ m (about } 17°)$$

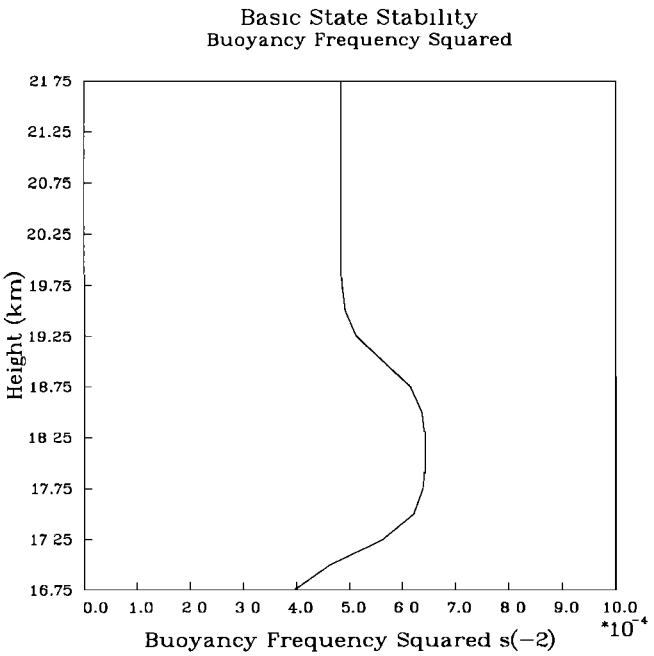

Fig. 10. Altitude dependence of the basic state buoyancy frequency squared $\left(\omega_b^2\right)$.

The finite difference version of (7) can then be solved for each wavenumber using standard methods and the result reconstituted using (6) to produce a three-dimensional perturbation field.

The altitude dependences of the three basic state quantities $\bar{u}$, $\bar{v}$, and ω_b^2 are shown in Figure 9 and Figure 10. The values of $\bar{u}$ and $\bar{v}$ are derived from a subjective combination of the aircraft observations and radiosonde data, while the buoyancy frequency squared ω_b^2 is derived from MTP measurements upwind of the observed gravity wave. The dissipation α is included in order to damp out critical layer phenomena with length scales comparable to the vertical grid size (50 m); it is constant with height with a value of (2 days)$^{-1}$. Since the vertical group speed of the gravity waves is such that they travel from the tropopause to 18.3 km in less than 2 hours, α should have no material effect on the phenomena of interest. In fact, use of substantially smaller and larger values of α had no discernible effect on the results.

The discussion in section 2.2 suggests that the convection acts as a barrier, forcing the lower stratospheric easterlies to pass over and around the tropospheric air mass that has been elevated by convective activity. In keeping with this basic hypothesis for gravity wave forcing, the lower boundary condition for (7) is expressed simply as

$$w_{bmn} = ik\bar{u}_b h_{mn} + il\bar{v}_b h_{mn} \tag{9}$$

where the "convective topography" h is

$$h(x,y) = \sum_{m=-M}^{M} \sum_{n=-M}^{M} h_{mn} e^{2\pi i(mx/L+ny/L)} = p_0 \,\mathrm{sech}^2\left(\frac{x-x_0}{L_x}\right)\mathrm{sech}^2\left(\frac{y-y_0}{L_y}\right) \tag{10}$$

We choose the mountain's horizontal length scales L_x and L_y and the coordinates of its center to be roughly consistent with the observed size and position of the regions of coldest GMS brightness temperatures in Figure 2. This image, taken at 0300 UT on February 3, is temporally closest to the time of the observed gravity wave in Figure 3, which was 0215 UT. Since the cloud top flight leg is at the edge of the region of low brightness temperatures, the maximum height p_0 of the "mountain" is unknown. We will find its value such that the calculated amplitudes at the upper flight leg (18.3 km, Figure 3) are in agreement with the observations.

Figure 11*a* shows the contours of h at the anvil top at 16.75 km. The chosen parameter values for this first simulation, called SS0300, are

$$L_x = 40\,\text{km} \tag{11}$$
$$L_y = 60\,\text{km} \tag{12}$$
$$x_0 = 138°\text{E} \tag{13}$$
$$y_0 = 13.35°\text{S} \tag{14}$$
$$p_0 = 400\,\text{m} \tag{15}$$

Note that the central latitude of the forcing (13.35°S) is also consistent with the aircraft measurements taken at 0245 UT in leg 2 near the anvil top (Figure 8). Figure 11*b* shows the modeled temperature field T and perturbation wind barbs at the overflight level (18.3 km) superimposed on the GMS brightness temperatures. The expected downwind slope of the gravity wave phase surfaces both north and south of the isolated

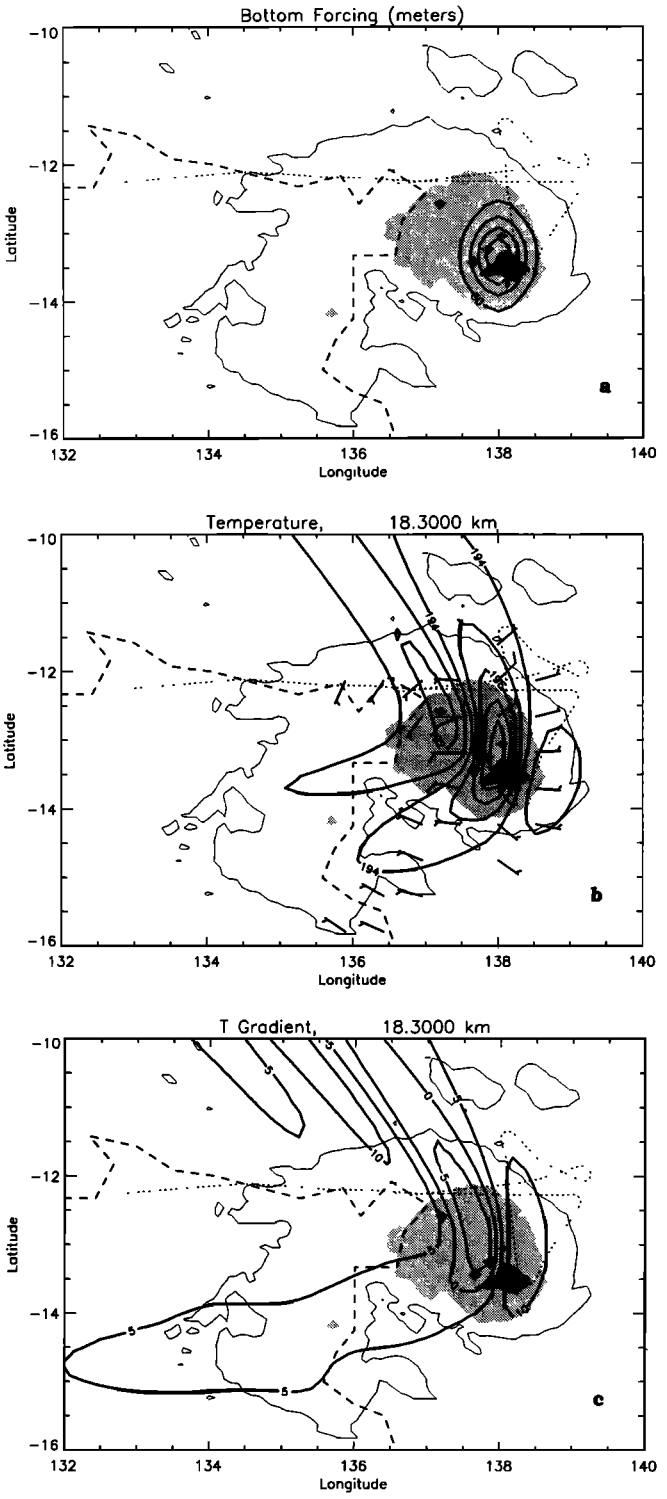

Fig. 11. Plan view of the results of the stationary simulation SS0300. (*a*) Contours of the convective "mountain" forcing (meters, thick solid lines) superimposed on the 0300 UT GMS IR image of February 3, 1987. The thin solid line outlines the region of IR brightness temperatures less than 223 K, while the light and dark shading define regions of IR brightness temperatures less than 202 K and 191 K, respectively. The dotted line represents the aircraft's flight path. (*b*) As in (*a*), except that the contours represent modeled temperatures at 18.3 km. Wind barbs (in knots) represent the modeled perturbation wind. No wind barb indicates perturbation winds of less than 5 knots (2.5 ms^{-1}). (*c*) As in (*a*), except that the contours represent modeled vertical temperature gradients at 18.3 km.

"mountain" forcing is clearly apparent. The perturbation wind vectors tend to be perpendicular to these phase surfaces, implying positive correlation of the zonal and meridional winds north of the forcing and negative correlation to the south. Another general feature of the model temperatures is that the amplitudes are larger north of the forcing than to the south. This is due to the fact that the mean wind vector turns clockwise with altitude, resulting in phase surfaces that are more nearly parallel to the wind vector north of the forcing; this implies a much smaller Doppler-shifted frequency $\hat{\omega}$. The vertical group velocity in this region

$$c_{gz} \sim \frac{\hat{\omega}^2}{\omega_b K} \tag{16}$$

is thus relatively small, resulting in a buildup of wave energy there [*Fritts*, 1984]. This buildup is even more apparent in Figure 11*c*, which shows the vertical temperature gradient T_z. The disturbance amplitude in the vertical temperature gradient T_z' is approximately the product of the local vertical wavenumber λ and the disturbance temperature T'. T_z' has contributions from both the amplitude and the phase variations of T' in the vertical, with only the phase variation accounted for here. However, since the amplitude of T' reaches a maximum near 18.3 km, the phase variation dominates in evaluating T_z'. Under slowly varying, hydrostatic conditions,

$$\lambda = \frac{\omega_b k}{\hat{\omega}} \tag{17}$$

Clearly, as one progresses northward from the forcing region, the phase surfaces will become more nearly parallel to the mean flow, the local Doppler-shifted frequency $\hat{\omega}$ will decrease, and the local vertical wavenumber $\lambda \sim T_z'/T'$ will increase.

A comparison of the observations with the steady state model output along the aircraft flight track at 18.3 km is shown in Figures 12*a* and 12*b*. If the modeled disturbance is shifted 0.5° eastward, its length scale, temperature amplitude, and zonal wind amplitude are in reasonable agreement with the observations. Interestingly enough, the forcing amplitude, 400 m, is similar to, if somewhat larger than, that found for the convective "mountains" in the 1980 Panama Water Vapor Exchange Experiment (*PI*). The model also reproduces the generally positive correlation between the meridional and the zonal wind perturbations (again, if shifted eastward by 0.5°). There are two major discrepancies between the model output and the observations. The first is the 0.5° westward shift of the modeled disturbance field. The second, and more important, discrepancy is that the amplitude of T_z' is about 70% too large. The observations indicate a value of 2.5 km^{-1} for the local vertical wavenumber $\lambda \sim T_z'/T'$, while the simulation value is 4.1 km^{-1}. The implication, based on (17), is that the local Doppler-shifted frequency is too small and the effective flow through the wave field too weak.

One explanation for these discrepancies is that the assumed convective forcing is both too far to the west and too far to the south. An eastward shift in the forcing would obviously "correct" the 0.5° westward phase shift error. A northward shift would place the aircraft observations in a region where the local vertical wavenumber $\lambda \sim T_z'/T'$ is smaller (because the phase surfaces are more nearly perpendicular to the mean flow; see above). There is some justification for assuming a forcing that is north and east of that assumed for SS0300. The region of brightness temperatures less than 191 K in the 0000 UT GMS image in Figure 1, for example, is both north and east of the

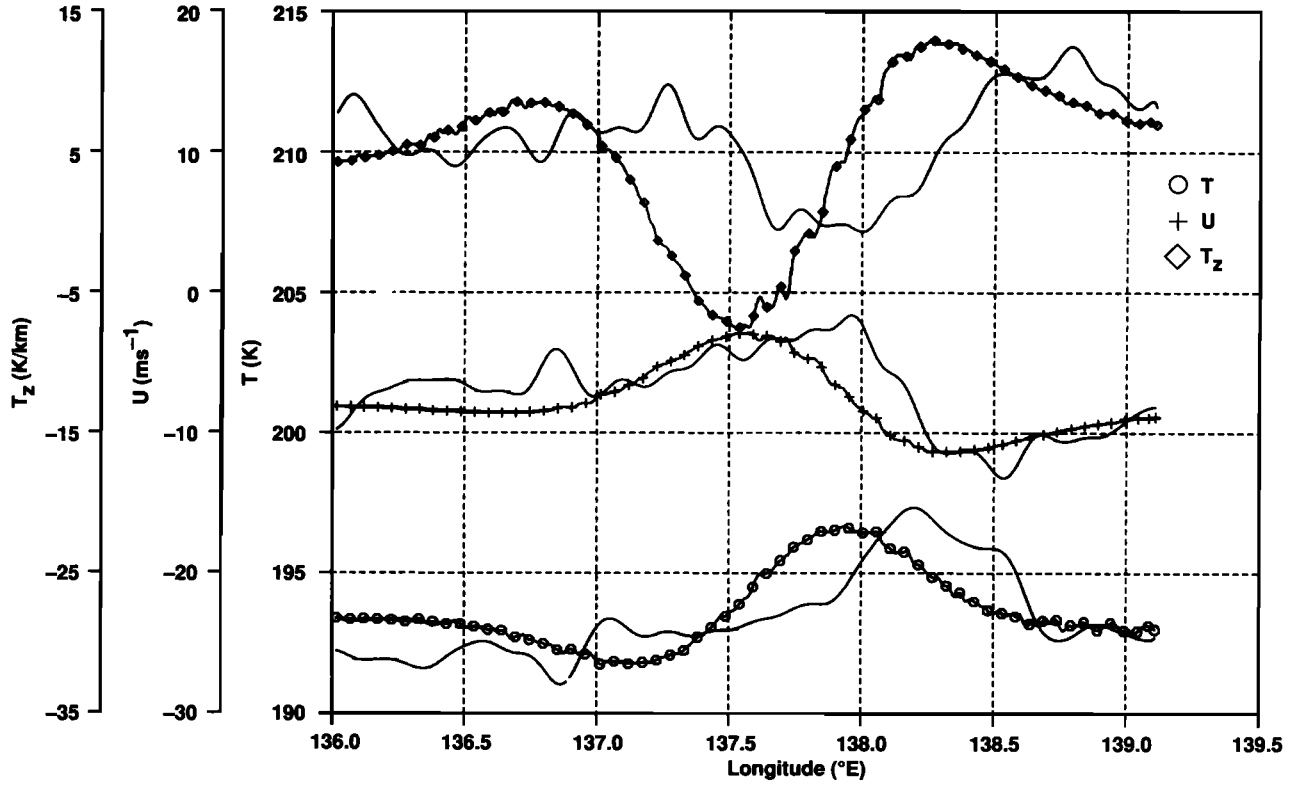

Fig. 12*a*. Comparison of aircraft observations from leg 1 and model results at 18.3 km for simulation SS0300. Each pair of curves consists of a solid line, representing the observations, and a line with a distinct symbol, representing the model results for that same meteorological parameter along the aircraft flight track. Diamonds, vertical temperature gradient; pluses, zonal wind; and circles, temperature. The small-scale structure in the model output curves is due to aircraft vertical motion.

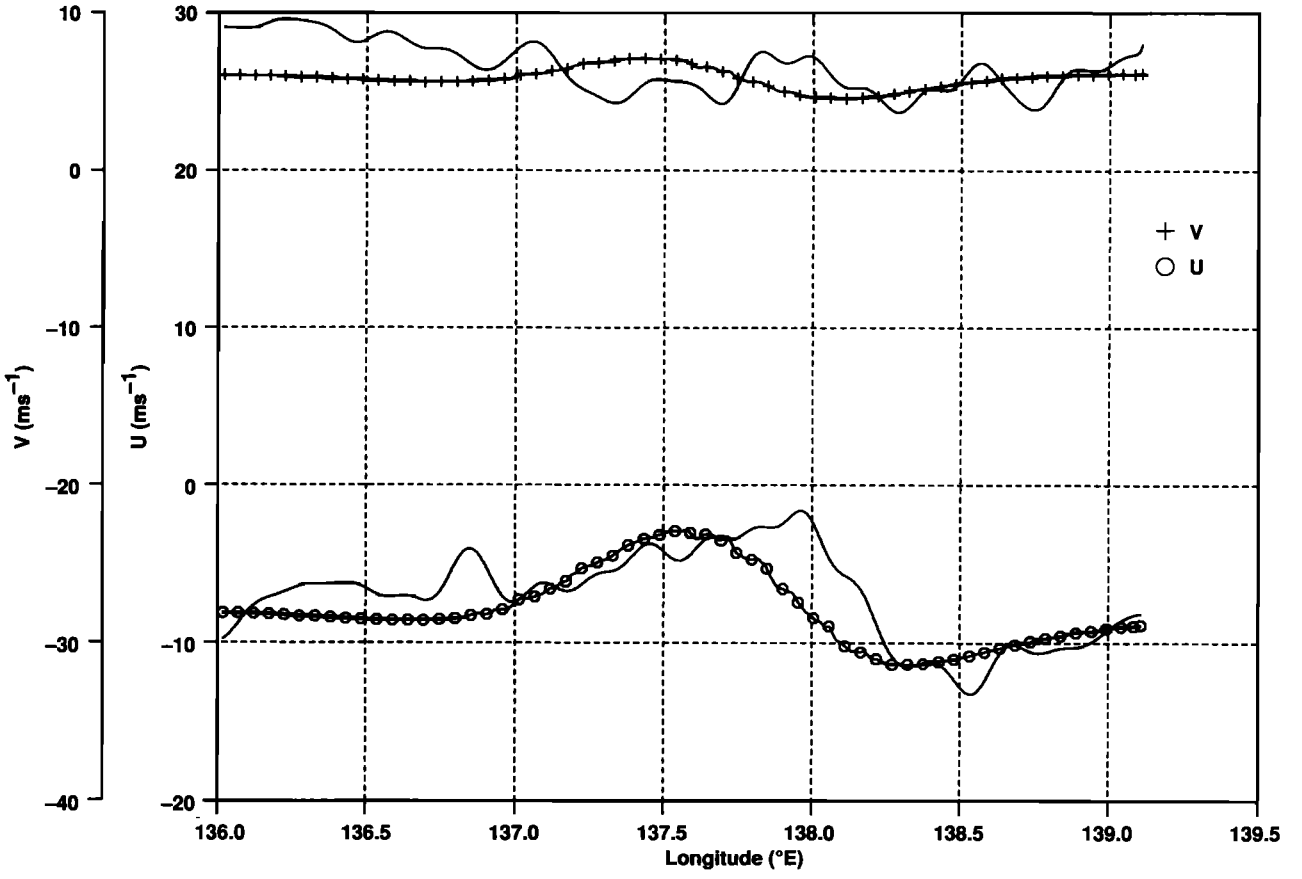

Fig. 12*b*. As in Figure 12*a*, except for meridional wind (pluses) and zonal wind (circles).

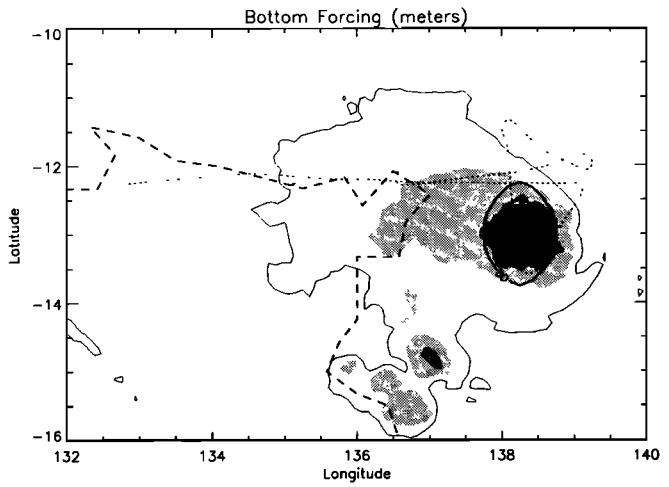

Fig. 13. As in Figure 11*a*, except for the 0000 UT GMS IR image on February 8, with a different location for the center of the convective forcing.

region with similar brightness temperatures in the 0300 UT image. A crude integration of the vertical group velocity (16) from the 16.75-km forcing level to the level of observations at 18.3 km using the basic state $\bar{u}$ and ω_b distributions with $\kappa = 5.7 \times 10^{-5}$ yields a transit time of 1-2 hours. Since the leg 1 observations were taken at about 0215 UT, the forcing that produced the observations represents conditions about 1-2 hours earlier, or 0015 to 0115 UT. Thus the 0000 UT GMS image may more accurately depict the location of the convective forcing responsible for the observed wave disturbance.

Figures 14*a* and 14*b* show the comparison of modeled and observed parameters for a forcing (Figure 13) more consistent with the 0000 UT GMS image. The parameter values for this case, SS0000, are the same as for SS0300 except

$$x_0 = 138.25°\text{E} \quad (18)$$
$$y_0 = 13.00°\text{S} \quad (19)$$
$$p_0 = 336\,\text{m} \quad (20)$$

The more eastward center of the forcing and its smaller latitudinal distance from the observations have eliminated the phase discrepancy of Figures 12*a* and 12*b*. However, as shown by the large disagreement with the observed vertical temperature gradient, the improvement in the simulation of the local vertical wavenumber T_z'/T' is small; the new value is 3.9 km^{-1} (as opposed to 4.1 km^{-1} for SS0300 and 2.5 km^{-1} for the data).

It is clear from this analysis that a stationary treatment of the problem consistently predicts excessively large vertical wavenumbers. This is a result of three factors: first, the low mean zonal wind speeds at 18.3 km as compared to the tropopause (16.75 km) level; second, the clockwise turning with altitude of the mean wind vector; and third, the placement of the convective forcing south of the aircraft observations. Moreover, each of these factors is consistently supported by the observations. The low wind speeds at 18.3 km are evident not only in the aircraft data, but in measurements from the surrounding radiosondes as well (Figure 3 and Figure 9). The same is true of the clockwise turning with altitude of the mean wind vector. Finally, the strongest convective forcing is almost certainly south of the leg 1 observation; this is evident not only from the satellite images but from the aircraft data on the leg 2 anvil pass and the positive correlation of the zonal and meridional winds on leg 1.

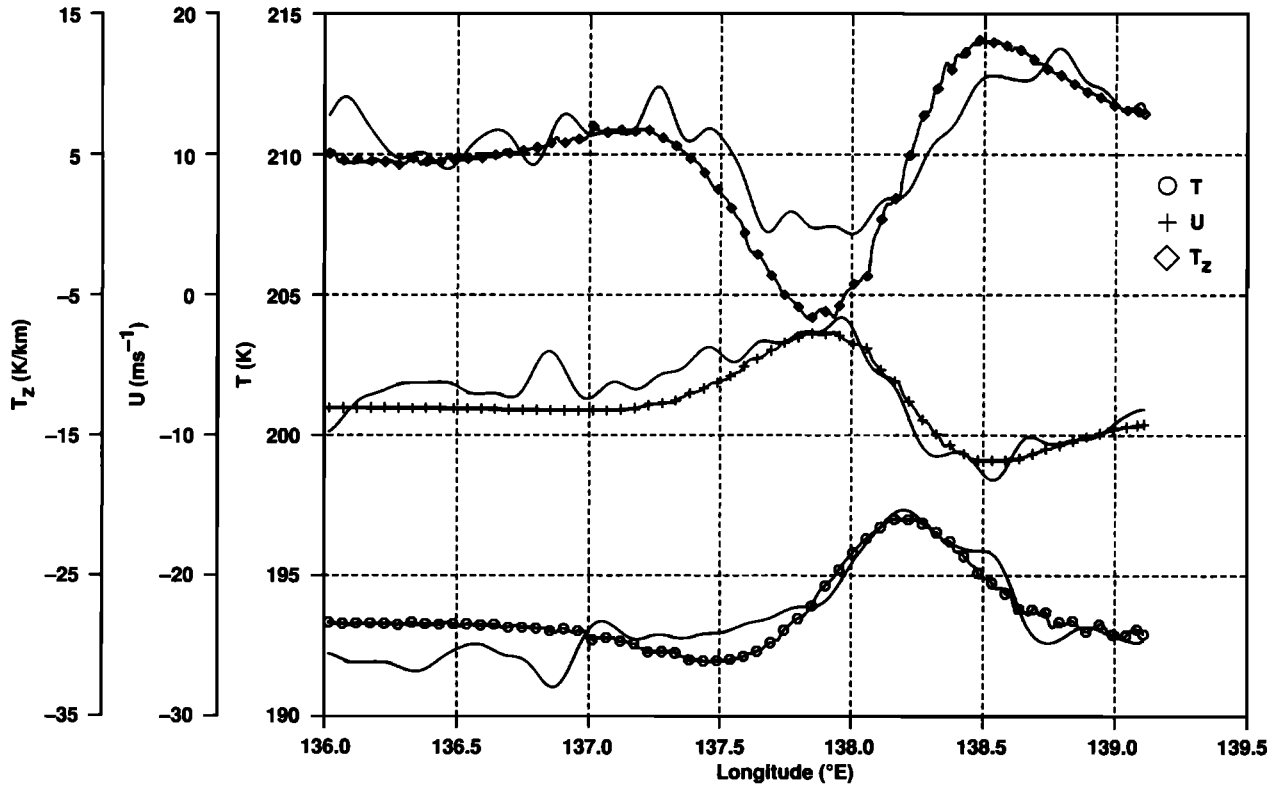

Fig. 14*a*. As in Figure 12*a*, except for simulation SS0000.

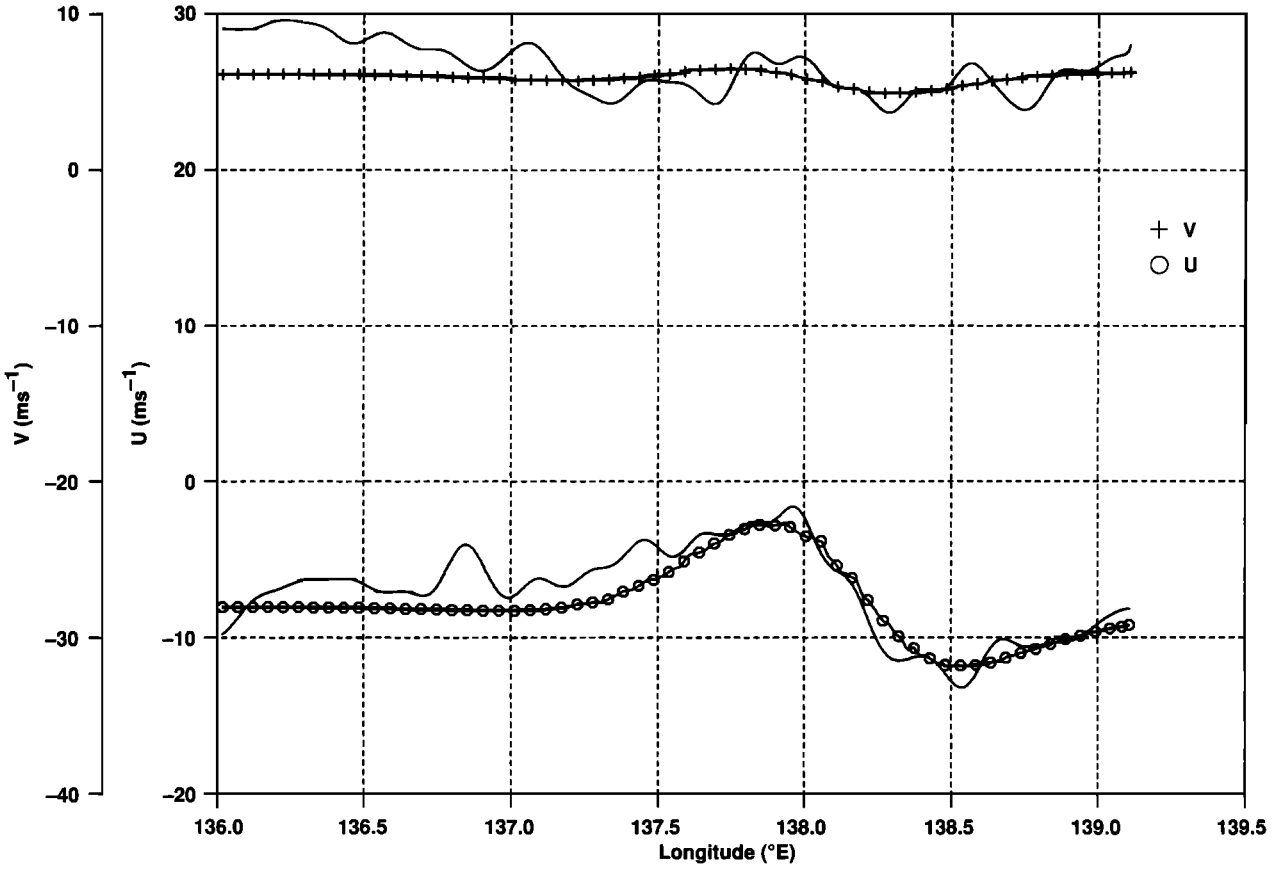

Fig. 14*b*. As in Figure 12*b*, except for simulation SS0000.

We can crudely calculate the increase in flow through the wave field required to reduce the vertical wavenumber to the observed value. Taking reasonable parameter values for the forced wave and mean flow properties at 18.3 km,

$$k = 5.2 \times 10^{-5}$$
$$l = 1.2 \times 10^{-5}$$
$$\kappa = 5.5 \times 10^{-5}$$
$$\omega_b = 0.025\ s^{-1}$$
$$\overline{u}\ \text{local} = -8\ ms^{-1}$$
$$\overline{v}\ \text{local} = 6\ ms^{-1}$$

and using (17) and (8), we obtain a value of 3.88 km^{-1} for λ, very close to the value from the complete linear solution. In order to reproduce the observed value of 2.5 km^{-1} the mean easterlies at 18.3 km would have to increase to $\overline{u}\ \text{local} = -12$ ms^{-1} from -8 ms^{-1}. As shown in Figure 3, such a large value is clearly well outside the range of uncertainty for the zonal wind.

4. Linear Transient Calculation

The preceding section has shown that the gravity wave in Figure 3 cannot be interpreted in terms of linear, stationary wave dynamics. The analysis also suggests that the wave may be moving eastward at ~4 ms^{-1}. However, there is little evidence that the underlying convective forcing exhibits such rapid movement during the times of interest. In Figure 1 the eastern edge of the T_{sat} < 191 K contour moves slightly eastward between the 2100 UT (February 7) and 0000 UT (February 8) GMS images, but the effective speed is less than 1.5 ms^{-1}.

An alternative approach would be to view the convective forcing as a transient "mountain" that temporarily lifts the bottom of the stratosphere by some distance and then recedes. This is similar to the "mechanical oscillator" mechanism of *Fovell et al.* [1992], except on a much larger scale. In *Fovell et al.'s* work single updrafts transiently impinge on the bottom of the stratosphere, raise and lower isentropic surfaces and thereby generate gravity waves. In this case, it is the growth and decay of an ensemble of updrafts over a few hours that raises and then lowers isentropic surfaces on a ~100 km scale. This would produce a transient, passing pulse of wave activity in the overlying stratosphere. Explaining the phenomenon this way is attractive since it is qualitatively consistent with the observed confinement in altitude (Figure 3, bottom window) and the decay in time (cf. Figure 3 and Figure 7). A wave generated by a convective pulse occurring 1-1.5 hours prior to the leg 1 observations will reach the 18.3-km level at the time of observation. Since much of the wave activity has passed through the lower levels already, small amplitudes at those levels are expected. Small amplitude at high altitudes during the leg 1 observations is also consistent with this conceptual model: the wave has simply not reached those altitudes yet.

There is evidence for these transient convective "mountains" in the observations. Though there is steadiness in the overall shape of the cyclone's cloud shield during the 12-hour period depicted in Figure 1, regions with brightness temperatures T_{sat} less than about 191 K expand and contract substantially. For example, at 1800 UT (February 7) there is a large region with T_{sat}<186 K centered just west of the southern end of the aircraft flight track. By 2100 UT this region has weakened substantially

and moved to the northeast. However, by 0000 UT (February 8) the region has moved slightly eastward and substantially revived; it then decays almost entirely by 0300 UT. This particular example may in fact be a good candidate to explain the aircraft observations. The stationary simulation in the previous section suggests that the location defined by the 0000 UT image is approximately correct. If the ~1- to 2-hour transit time is taken into account, a forcing maximizing at 0000 UT will produce maximum amplitude at 18.3 km as late as about 0200 UT. This is certainly close enough to the observed time of 0215 UT, especially since the 3-hour time resolution of the GMS images implies a ~1-hour uncertainty in the time of the convective forcing.

The transient forcing can be crudely represented by including a time dependence in the expression for the convective "mountain" (10).

$$h(x, y, t) = p_0 g(t)\,\mathrm{sech}^2\left(\frac{x-x_o}{L_x}\right)\mathrm{sech}^2\left(\frac{y-y_o}{L_y}\right) \qquad (21)$$

with

$$g(t) = 0 \qquad t < t_0$$

$$g(t) = \tfrac{1}{2}\left(1-\cos\left(\frac{2\pi(t-t_o)}{\tau}\right)\right)^{3/2} \qquad t_0 < t < t_0+\tau$$

$$g(t) = 0 \qquad t > t_0+\tau$$

Here the time dependence is a modified single sinusoid with a period of τ. This is identical to the time dependence used by *Pl.* The 3/2 exponential dependence is designed to minimize numerical instability in the time integration from the "start-up" of the forcing function. Eastward movement of the forcing, if any, can be included in this formulation by transforming into the reference frame of the moving convective "mountain"; essentially, (21) is used, except with the basic state easterlies augmented by the assumed motion of the convective system.

The stratospheric response to such a forcing will include a full spectrum of phase speeds, not just the zero phase speed. This can be seen in Figure 15, which shows the time and area-integrated vertical flux of zonal momentum $\overline{\rho u' w'}$ as a function of zonal phase speed excited by a disturbance described by equation (21) with p_0 = 400 m. Vertical flux of zonal momentum is chosen since it is independent of altitude under quasi-steady, nondissipative conditions. It is derived by evaluating w' from (9) and calculating u' from (2). We have assumed that the disturbance is not moving and that the flow over it is easterly with a tropopause zonal wind speed of $\bar{u}_t$ = -23.5 ms^{-1} (the zonal wind component at the tropopause from Figure 9). The two curves are for two different values of τ, 4.5, and 6 hours. Unlike the stationary case, which would consist of a delta function at zero phase speed, the momentum flux has a broad spectrum of phase speeds. Moreover, the maximum in the momentum flux is not found at zero phase speed but is displaced to westerly phase speeds of about 1-2 ms^{-1} for τ=6 hours and 3 ms^{-1} for τ = 4.5 hours. Momentum flux values comparable to values at the maximum are found at westerly phase speeds of up to ~5 ms^{-1}. The implication is that a transient convective mountain described by equation (21) could produce waves with westerly phase speeds sufficiently large to account for the small vertical wavenumber implied by the observed ratio of T_z'/T'. Moreover, any eastward movement of the forcing would enhance this effect; the curves in Figure 15 would be shifted to the right by the speed at which the forcing is moving.

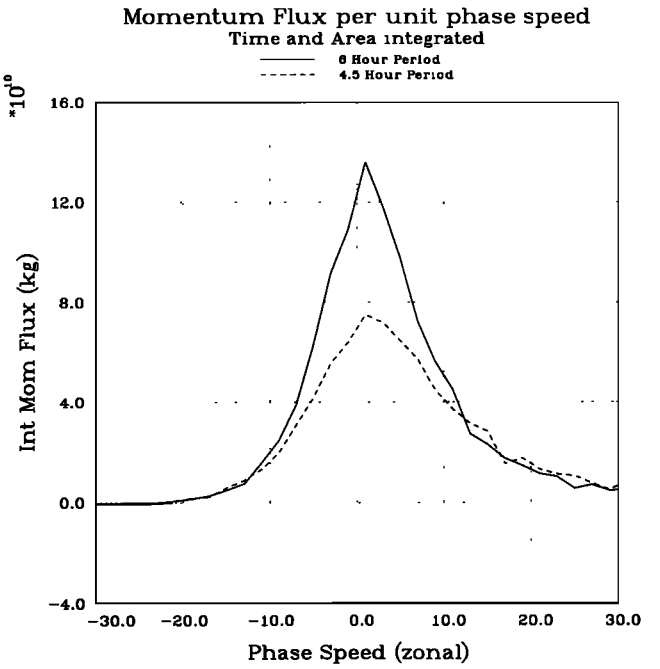

Fig. 15. Time-and area-integrated vertical flux of zonal momentum per unit phase speed interval excited by the disturbance described in the text. Units are kilograms.

One unresolved issue is that of the appropriate forcing period τ. It is not possible to fully resolve periods less than about 12 hours with 3 hourly satellite images, yet the spotty time continuity in the mesoscale cloud features clearly suggests that shorter forcing periods are present. *Danielsen* [1982], for example, using half hourly IR GOES images, estimated periods of 5 hours for mesoscale cell structures in the Gulf of Panama. We will treat the period τ as a parameter and perform simulations for 4.5-and 6-hour forcing periods, both with and without the 1.5ms^{-1} eastward translation speed suggested by the satellite images. The forcing amplitude p_0 is set to reproduce the magnitude of the temperature disturbance in Figure 3 at the time when the vertical wavenumber at the aircraft location is roughly consistent with the observations. The final observational constraints will be consistency of the temporal evolution of the model temperature field along the aircraft flight track with (1) the satellite measurements of the time of the forcing and (2) the observed decay of the disturbance after 0215 UT (Figure 3).

To simulate the transient development, we will integrate the linearized equations of motion for a time ~1.5 τ and watch the development at 18.3 km. As with the stationary simulation, the variables can be represented as double Fourier series, with each Fourier component now dependent on time as well as height. Since the equations are linear, each Fourier component can be integrated in time independently; at desired time intervals the Fourier components are reconstituted to produce the three-dimensional spatial distribution for a given variable. The time-stepping scheme is implicit, with time steps of 3 min and time filtering every 20 min. It is similar to that used by *Coy* [1984].

Figure 16 shows the temporal development of the temperature field at 18.3 km for a forcing of the form specified by equation (21) with τ = 4.5 hours, p_0 = 600 m, and a translation speed u_T = 1.5 (simulation TR4.5/1.5: TR denotes transient, 4.5 denotes 4.5 hours, and 1.5 denotes 1.5 ms^{-1} translation speed). The

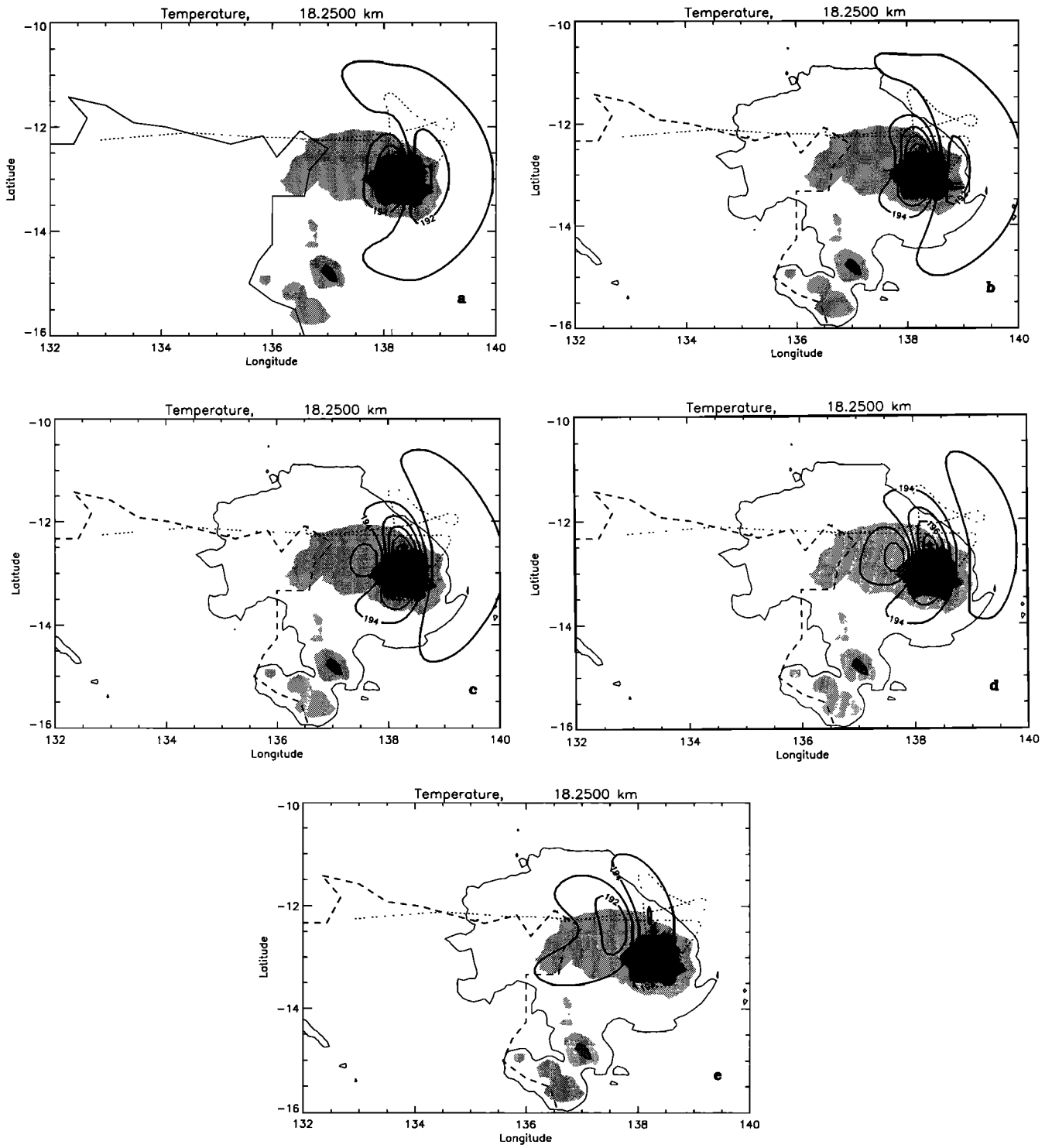

Fig. 16. Plan view of the results of simulation TR4.5/1.5 at 18.3 km at five different times: (*a*) 0.25 hour; (*b*) 0.75 hours; (*c*) 1.25 hours; (*d*) 1.75 hours; and (*e*) 3.25 hours. Contours are plotted on the 0000 UT GMS infrared image of February 8, 1987. Shading and thin solid contour are as in Figure 11.

geographical center of the forcing, which is the same for all the transient simulations, is the same as that for the steady, stationary simulation SS0000 (Figure 13). The times given in the figures are measured from the time of maximum elevation of the "convective mountain". The series of figures illustrates three basic points. First, the maximum overall peak-to-peak temperature disturbance at 18.3 km occurs about an hour after the maximum convective "mountain" height has been achieved (between realizations (*b*) and (*c*) in Figure 16). This is roughly consistent with the crude transit time calculation based on vertical group velocity mentioned in the previous section. About one hour later (realization (16*d*)) the maximum amplitude has been reduced by 25%. Second, the temperature disturbance spreads northward and southward with time, with a significant

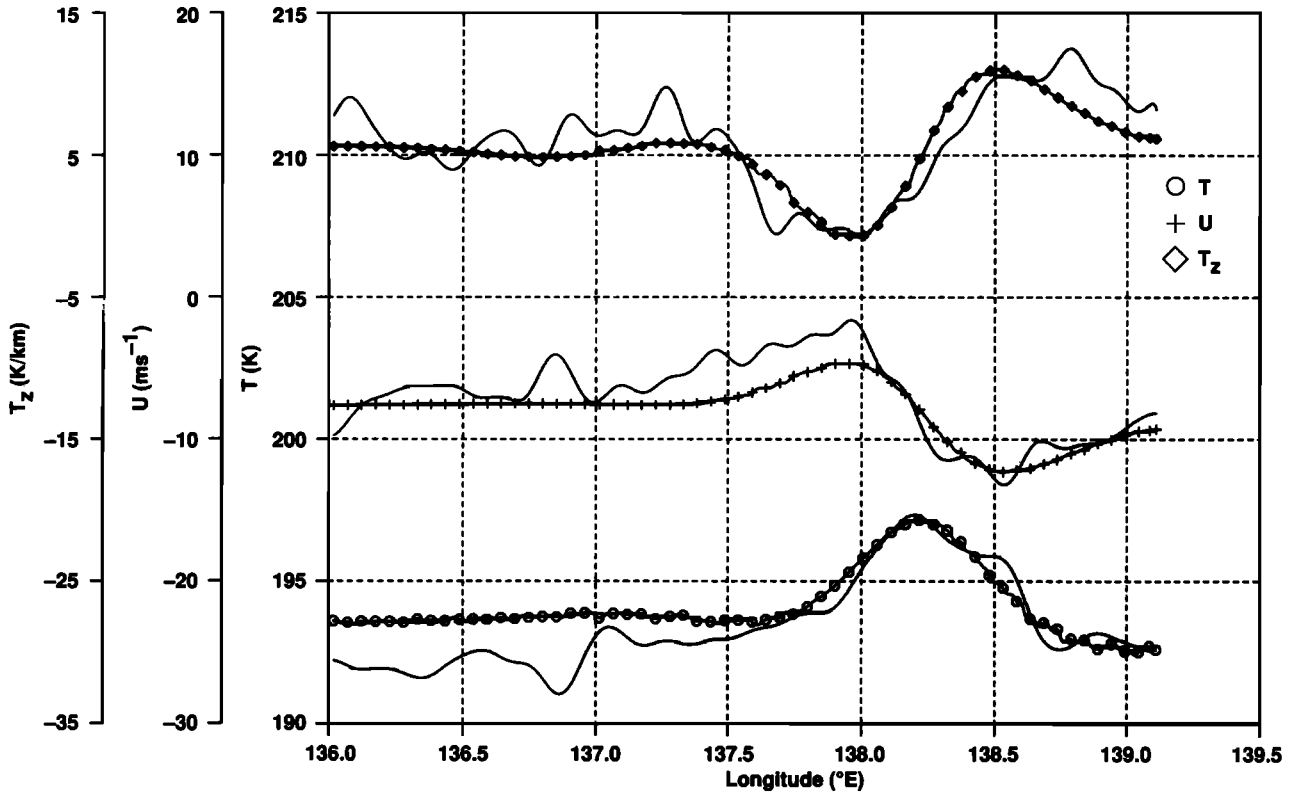

Fig.17. As in Figure 12*a*, except for simulation TR4.5/1.5 at t=1.25 hours.

northward shift apparent by t = 1.75 hours. This northward shift is due to the slower vertical group velocity of the northward propagating components, a direct consequence of their smaller Doppler-shifted phase speed, due to the turning of the mean wind with altitude. The northward shift implies that maximum temperature amplitude at the aircraft location north of the forcing occurs after the overall 18.3-km maximum peak-to-peak amplitude. Third, there is a clear eastward phase propagation with time. In the 1.5 hours after t = 15 min (realization (16*a*)), the temperature maximum moves about 0.17° eastward, implying a phase speed of 3.5 ms^{-1}. Note that this is faster than the 1.5 ms^{-1} eastward translation of the forcing by about 2 ms^{-1}. It is also roughly consistent with the phase speed of maximum momentum flux in Figure 15 (after the 1.5 ms^{-1} translation speed is added).

Figure 17 shows the comparison of the simulated and observed disturbances along the leg 1 flight track at the time of maximum peak-to-peak simulated leg 1 temperature amplitude (t = 1.25 hours, Figure 16*c*). The agreement is remarkably good, with the only measurable discrepancy being in the zonal wind perturbation. Assuming that the t=1.25-hour model realization (Figure 16*c*) corresponds to the leg 1 observations at 0215 UT, this implies a forcing peak at 0100 UT, which is roughly consistent with the satellite data when the error due to the 3-hour time resolution is allowed for. Most importantly, the time evolution of the model temperature disturbances shown in Figure 19*a* is at least qualitatively consistent with the observed decay of the disturbance between 0215 UT (Figure 3) and 0420 UT (Figure 7); by t = 3.25 hours (Figure 16*e*), two hours after the t = 1.25-hour realization (Figure 16*c*), the magnitude of the peak-to-peak temperature disturbance has decreased to 3.7 K, roughly consistent with the observed decline in peak-to-peak temperature disturbance magnitude (Figure 7).

Figure 18 shows the actual comparison between the t = 3.25 hour realization and the second 18.3-km pass over the cyclone at 0420 UT (Figure 7). Though the temperature disturbance magnitudes compare well, the phases are in clear disagreement, which cannot be explained by errors in the aircraft position (recall that this was estimated by dead reckoning due to INS failure; see section 2). Moreover, there is no evidence for the model-predicted dip to -5 K/km lapse rates near 138°E in the observations. One explanation for this disagreement is that nonlinear effects, such as wave breaking, have become sufficiently important by this time to violate the linear assumptions in the model. That nonlinearity should increase with time is expected, since it is the waves with the lowest eastward phase speeds that are the most nonlinear (because the linear advection and time derivative terms are smallest). In fact, the linear model predicts very low values of the Richardson number (0.4) very near the aircraft location late in the simulation (2.25 hours). The fact that the temperature disturbance in Figure 7 is irregular rather than a smooth wave as in Figure 3 is also consistent with the scenario of wave breaking as the slower moving waves reach the 18.3-km (aircraft) level.

Figures 19*a* and 19*b* show the sensitivity of the time evolution of the peak-to-peak temperature disturbance and effective vertical wavenumber along the flight path to variations in the forcing period τ and the translation speed. The TR4.5/1.5 simulation is shown, along with three others involving combinations of a different τ (6 hours) or a different eastward translation speed (0 ms^{-1}). Clearly, the time evolution of the effective vertical wavenumber is fairly insensitive to the forcing period and very insensitive to the translation speed. On the basis of vertical wavenumber alone, any of the four cases at t = ~1-1.5 hours would be consistent with the observations. In

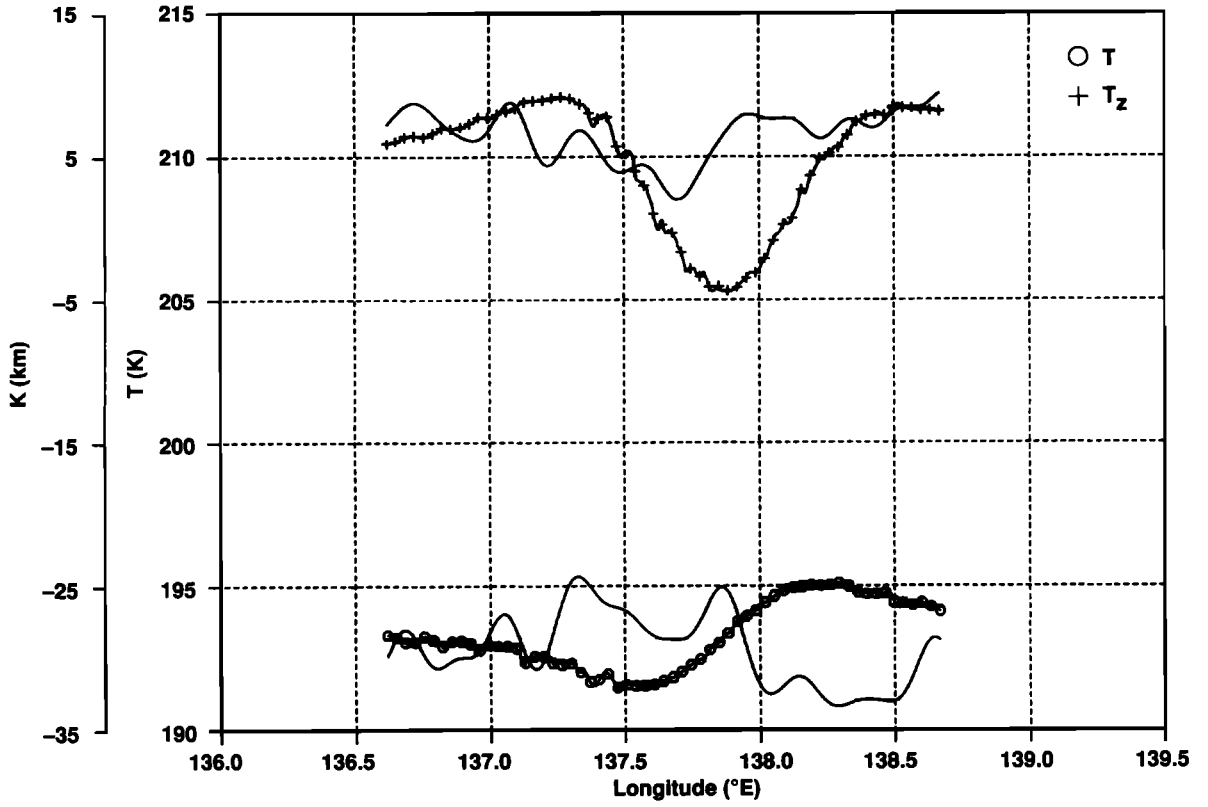

Fig. 18. Comparison of aircraft observations from the second 18.3-km leg (Figure 7) and TR4.5/1.5 model results at 18.3 km and t=3.25 hours. Each pair of curves consists of a solid line, representing the observations, and a line with a distinct symbol, representing the model results for that same meteorological parameter along the aircraft flight track. Pluses, vertical temperature gradient; and circles, temperature.

contrast, the temperature disturbance evolution is quite sensitive to the parameters. Of the four simulations, only TR4.5/1.5 shows any decrease at all in temperature amplitude between t = ~1 hour (when vertical wavenumbers are in agreement with observations in Figure 3) and t = 2.75 hours.

Table 1 summarizes the observations and the steady state and transient model results for leg 1. The times listed for the transient model runs were those at which the vertical wavenumber matched the observations; as indicated above, the forcing amplitudes were chosen to approximately match the observed temperature amplitudes at those times. The most important point of the table is that the forcing amplitudes required to produce the observed temperature amplitudes are substantially larger for the transient cases than for the steady

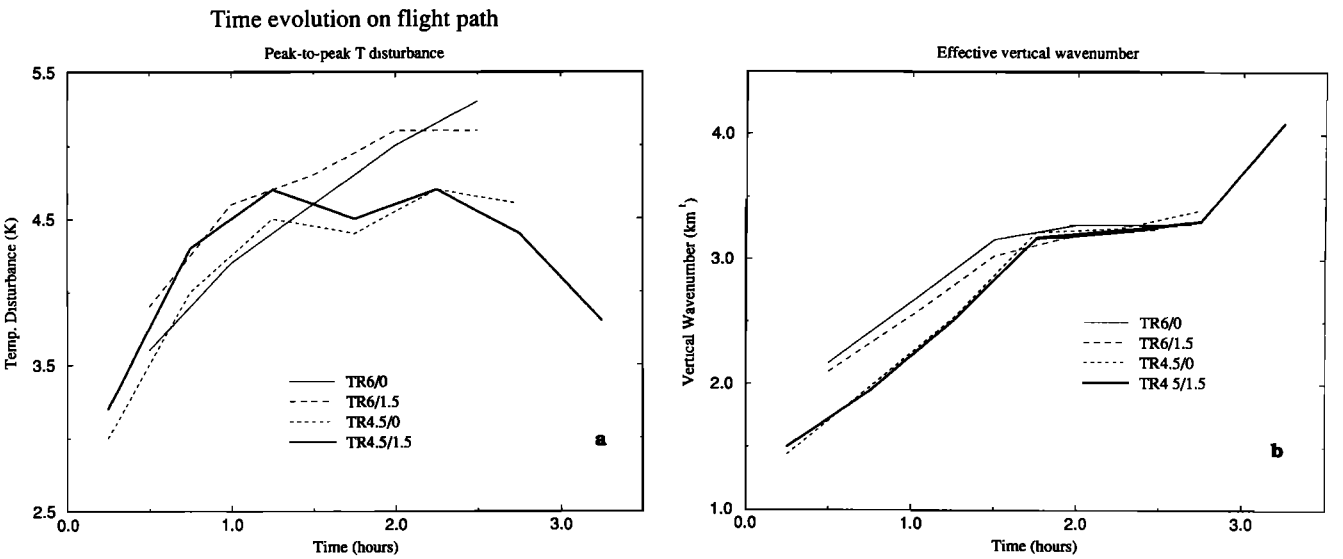

Fig. 19. (*a*) Evolution of the peak-to-peak temperature disturbance of four different linear transient simulations described in the text. The temperature disturbances are evaluated along leg 1 in Figure 2. Times are measured from the time of maximum convective forcing amplitude. (*b*) As in (*a*), except for the effective vertical wavenumber.

TABLE 1. Peak-to-Peak Values Along the Flight Path

Case	Time, hours	T', K	u', ms^{-1}	λ_{eff},km^{-1}	p_0,m
Observed	...	4.8	8.8	2.5	...
SS0300	...	5.0	8.5	4.07	400
SS0000	...	5.0	9.0	3.90	336
TR6/0	1.0	4.2	7.0	2.66	540
TR6/1.5	1.0	4.6	7.6	2.55	540
TR4.5/0	1.25	4.5	7.4	2.53	600
TR4.5/1.5	1.25	4.7	7.7	2.51	600

Values of the meteorological parameters along the aircraft flight path for the observations, linear steady state simulations, and linear transient simulations. T' denotes the peak-to-peak temperature disturbance, u' the peak-to-peak zonal wind disturbance, and λ_{eff} the effective vertical wavenumber T_z'/T'. The forcing amplitude for the simulations p_0 is also included. The times for the linear transient simulations are those with the best agreement with the observed vertical wavenumber.

state cases. This is nearly a factor of 2 if SS0000 is compared with the TR4.5/1.5, the transient case having the best agreement with the observations. For the 6-hour forcing cases the temperature amplitudes indicated in the table are not the largest attained during the integration. Even so, if the maximum amplitudes from Figure 19 are considered and the forcing is scaled to make these maxima match the observed amplitude of 4.8 K, the forcing amplitudes would still be larger than for the steady cases by factors of 1.4 (TR6/0) and 1.5 (TR6/1.5).

An important caveat, obvious from an inspection of Figure 16*c*, is that the model temperature amplitude in Figure 17 is quite sensitive to the relative latitudinal positions of the flight track and the forcing region. If the flight track were shifted 20 km to the south, for example, the forcing amplitude p_0 required for agreement with the observations would be 500 m instead of 600 m. Given the time resolution problems of the GMS images on the time scales of interest, the uncertainty in these relative positions is at least this large (the uncertainty due to the size of the GMS satellite pixels alone is about 10 km). Since the horizontal gradients in the steady state fields (Figure 11*b*) are not nearly as large, the enhancement of forcing amplitudes due to the inclusion of transient effects may be overestimated in Table 1.

5. Discussion

The size of these inferred forcing amplitudes has significance for the momentum budget of the tropical stratosphere. *P1* calculate the convective gravity wave drag in the middle and upper stratosphere based on the hypothesis that the waves are produced by convective topography of the form (21). In their formulation the drag is proportional to a weighted sum of the total impulse from each convective system, with the number of convective systems calculated from global cloudiness statistics. The total impulse from each system depends on the time scale τ, the spatial scales L_x and L_y, the tropopause zonal wind $\bar{u}_t$, and the square of the convective topography height p_0. This squared dependence arises from the linear dependence of both u' and w' on p_0 and the direct proportionality of the impulse to the vertical momentum flux $\overline{u'w'}$.

P1 assumed a characteristic forcing amplitude of 300 m for mesoscale convection with similar horizontal and time scales to those used in this case study. Extrapolating to the global tropics, *P1* concluded that gravity wave momentum fluxes produced by tropical mesoscale convection could account for perhaps a third of the westerly phase of the semiannual oscillation (SAO) but barely a tenth of the easterly phase of the quasi-biennial oscillation (QBO). (This was subject to a number of uncertainties, the most important of which is a factor of 3 or 4 in the global cloudiness statistics.) If, based on this study, we increase the forcing amplitude everywhere in the tropics from 300 m to a (fairly conservative) value of 450 m and held all other things equal, a doubling in the momentum flux would result. This would imply a nearly dominant role for mesoscale gravity waves in the westerly phase of the semiannual oscillation and a significant (20%) role in the easterly phase of the QBO. It is thus important to ask the following questions: (1) Is there any other evidence for forcing amplitudes of the above implied magnitudes from the STEP data set? (2) Is all the gravity wave momentum flux generated by convection during STEP actually transmitted to the middle and upper stratosphere? and (3) If some of the gravity waves are absorbed in the lower stratosphere, what impact do they have?

Figure 20 shows vertical profiles through the anvil top of tropical Cyclone Damien (Figure 21) at two locations. The profiles are taken on descent into the main portion of the anvil at 0300 UT on February 4 (Figure 20*a*; the triangle in Figure 21) and on ascent through a rainband on the northeast corner of the main anvil at 0345 UT (Figure 20*b*; the square in Figure 21). The satellite image is taken at 0300 UT; it is thus a good representation of conditions at the times the vertical profiles were taken. The potential temperatures within the anvil regions of both profiles are nearly constant with altitude and identical at about 368 K, with nearly constant and typically tropospheric ozone mixing ratios of less than 40 ppbv. In both cases the tropospheric air is capped by a sharp inversion, above which is stratospheric air. The important and obvious difference between the two profiles is that the rainband anvil (0345 UT profile) is 600-700 m higher than the main anvil (0300 UT profile). One reasonable interpretation is that mesoscale convection raises the tropopause by distances of this magnitude, consistent with the 500- to 600-m distances inferred in section 4. This is subject to the caveat that the convective topography on the cyclone scale is not known; that is, some portion of the difference in tropopause altitudes between the profiles in Figures 20*a* and *20b* may be due to variations on the scale of the cyclone's cloud shield as a whole [see *Danielsen*, this issue]. Nevertheless, Figure 20 represents additional evidence for up to 600-m variations in tropical convective topography.

One factor that reduces the gravity wave momentum fluxes to the middle and upper stratosphere is wave breaking within and

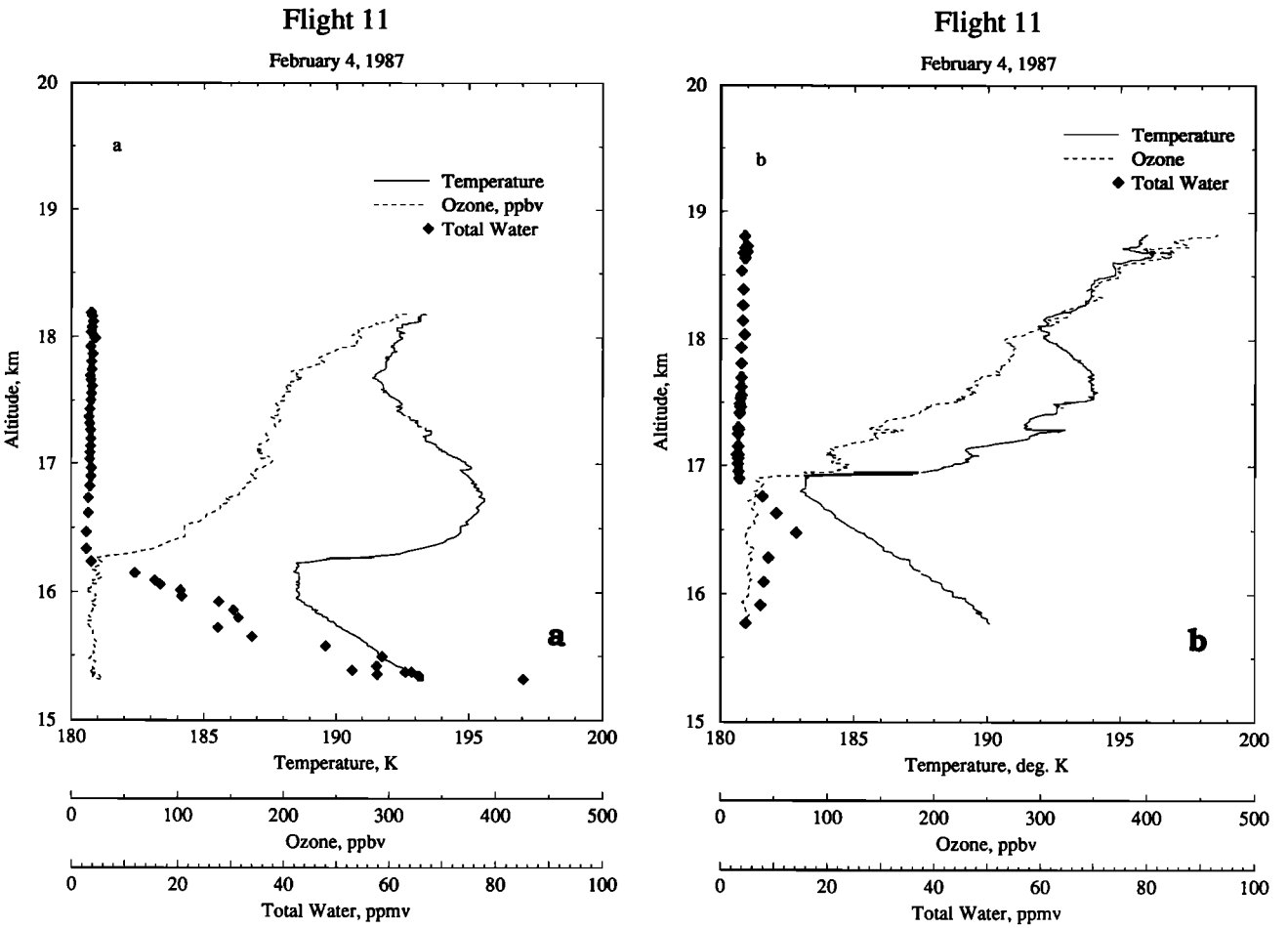

Fig. 20. (*a*) Vertical profile of temperature (solid line), total water (diamonds), and ozone mixing ratio (dashed line) at the west end of Cyclone Damien on February 4, 1987 (STEP Flight 11). (*b*) As in (*a*), except for the east end of Cyclone Damien.

absorption by the lowest 5 km of the stratosphere. That this might be a factor is apparent from a comparison of Figure 9 and Figure 15. Figure 9 shows a substantial weakening of the easterly winds above the tropopause, from -23 ms^{-1} to -8 ms^{-1}. Thus in an atmosphere with purely zonal mean winds, gravity waves with phase speeds less than -8 ms^{-1} will reach critical levels below 18 km and will presumably be absorbed through wave breaking near those critical levels. Waves with these phase speeds account for less than 10% of the total impulse produced by a convective system (Figure 15), so their absorption by the lower stratosphere would not affect the momentum flux to the middle and upper stratosphere significantly. However, waves do not need to attain infinite vertical wavenumber (that is, reach a critical level) in order to break. Depending on wave amplitude, some waves with finite vertical wavenumber (or zonal phase speeds greater than -8 ms^{-1} in this case) will almost certainly experience breaking near the 18-km wind minimum.

Evidence for wave breaking has already been presented in the previous section, with the implication that waves with vertical wavenumbers $\lambda > 3.2\,km^{-1}$ may break (and be absorbed) in the wind minimum region near 18.3 km. Using the hydrostatic dispersion relationship

$$c_d = \hat{\omega}/\kappa = \omega_b/\lambda \qquad (22)$$

we estimate that waves with Doppler-shifted phase speeds c_d < 7.5 ms^{-1} will break. Since $\bar{u}$ = -8 ms^{-1} at the point of minimum wind near 18 km, this indicates, for purely zonal waves in an atmosphere with a purely zonal mean wind, that waves with zonal phase speeds less than -0.5 ms^{-1} would break near the -18 km wind minimum. (This -0.5ms^{-1} figure is also roughly consistent with the possible nonlinearity of the steady, cyclone scale feature at 18.3 km discussed in section 2.3). Taking the area under the dashed curve in Figure 15 having phase speeds less than -2 ms^{-1} (which accounts for the 1.5 ms^{-1} translation speed used for the TR4.5/1.5 case), we estimate that perhaps a fifth to a quarter of the total impulse produced by this convective event is absorbed in the 18.3-km wind minimum region.

Obviously, this will reduce the impact of mesoscale convective gravity waves on the middle and upper stratosphere. More importantly, it will probably affect the upward flux of westerly momentum more than the upward flux of easterly momentum. Figure 22, taken from *P1*, shows the impulse produced by a convective mountain with a lifetime of 5 hours and a maximum height of 300 m as a function of tropopause zonal wind speed. Of note here is that significant fluxes of easterly momentum by convectively induced mesoscale gravity waves are produced primarily in regions of weak tropopause winds; conversely, the large fluxes of westerly momentum are produced in regions of strong easterly tropopause winds. These strong easterly jets are more likely to be overlain by westerly shear zones (as in the STEP region) than weak winds are to be overlain by easterly shear zones (unless the QBO is fully descended). Thus

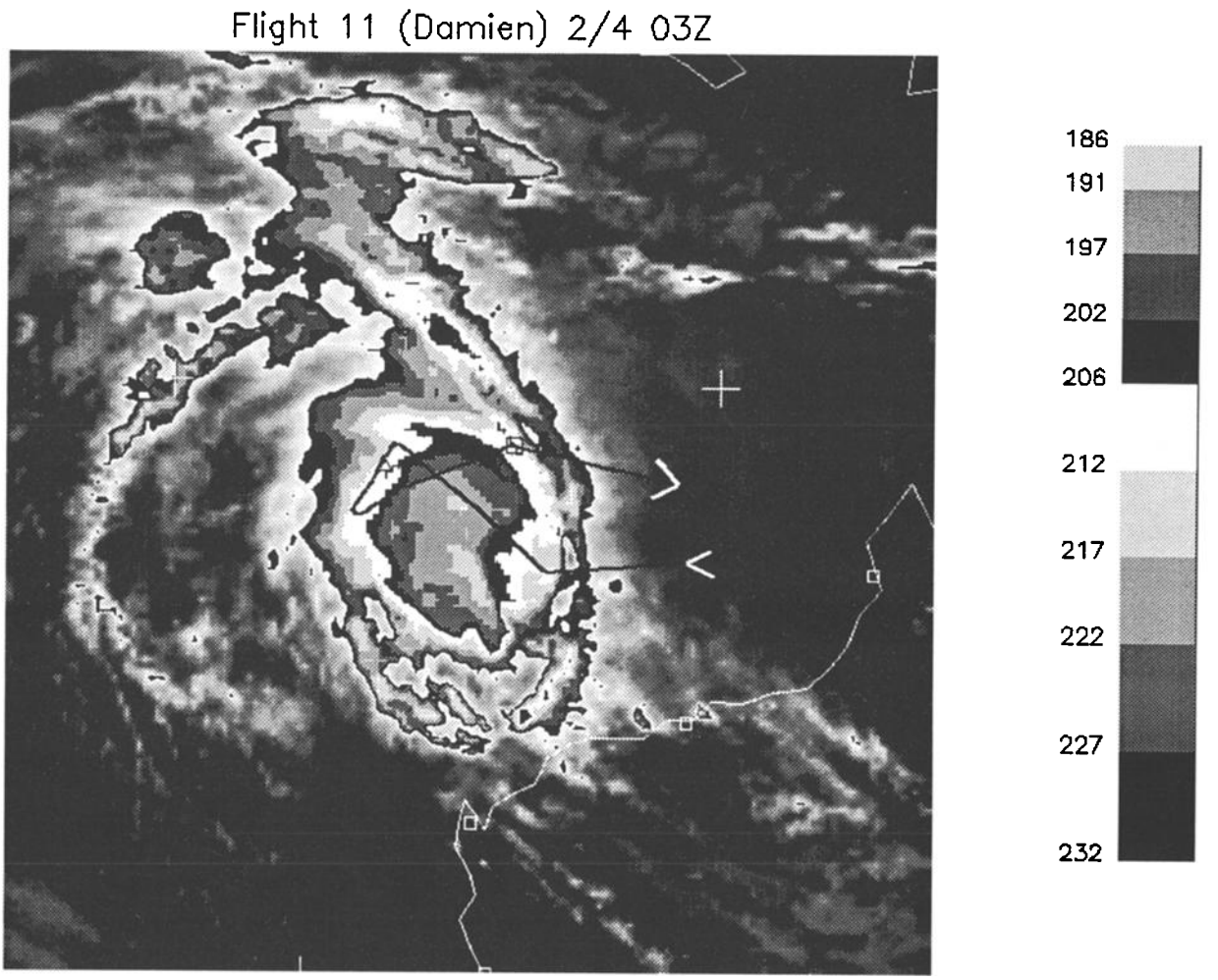

Fig. 21. Enhanced GMS infrared satellite image for 0300 UT on February 4, 1987.

absorption in the lower stratosphere will primarily affect waves with momentum fluxes that impact the westerly SAO.

Wave breaking near 18 km in the STEP region not only reduces accelerations in the upper stratosphere but also may have an impact on the lower stratospheric circulation, at least on a regional basis. We can estimate this impact by assuming (1) that this one quarter of the westerly impulse is absorbed in the scale height (about 6 km) above 18 km and (2) that none of the gravity waves in question radiate horizontally out of the STEP region. The effective zonal force in the 18- to 24-km region A_C (in acceleration units) will be

$$A_c = \frac{I_c \cdot N_c}{M} \tag{23}$$

Here I_C is the impulse absorbed per mesoscale convective system, N_c is the number of such systems per unit time and area, and M is the mass of the affected part of the lower stratosphere per unit area. We calculate I_c by integrating the dashed curve in Figure 15 between -15 ms^{-1} and -2 ms^{-1} and then multiplying by 1.25 to account for the higher estimated topography amplitude (p_0 = 450 m versus 400 m assumed for Figure 15). $N_c = f/AT$, where f is the fractional convective cloudiness (we choose f = .05 as in the work of *PI*) and AT is the "area time" occupied by a single system, essentially

$$AT \sim \frac{1}{2}\,\tau\,\pi\,L_x\,L_y \tag{24}$$

$M = 0.63\,\rho_0 H$, where ρ_0 is the density at 18 km. The three components of the right-hand side of (23) are:

$$I_C = 3.7 \times 10^{11}\ \text{kg ms}^{-1} \tag{25}$$
$$N_C = 5.5 \times 10^{-16}\ \text{m}^{-2}\text{s}^{-1} \tag{26}$$
$$M = 480\ \text{kg m}^{-2} \tag{27}$$

which implies that the effective zonal force is approximately 0.035 $ms^{-1}\,d^{-1}$. This is about a fortieth the value of typical time changes in horizontal wind associated with planetary scale tropical waves (such as the Kelvin and mixed Rossby-gravity waves [see *Holton*, 1975, p. 23]). However, wind fluctuations due to waves are reversible, while gravity wave breaking is not. Thus it is more appropriate to compare this calculated zonal force to another irreversible process, such as diabatic heating. A 1 K/d diabatic cooling rate (Q) above the clouds [*Ackerman et al.*, 1988] implies, from the thermodynamic equation, a downward vertical velocity of

$$\overline{w} = \frac{RQ}{\omega_b^2 H} = .001\ \text{ms}^{-1} \tag{28}$$

Over a scale height this implies a horizontal divergence of about 1.5 x $10^{-7}s^{-1}$. The horizontal divergence due to gravity wave breaking is approximately $A_C\tau/L$, where L is the zonal scale over which convective activity (and presumably gravity wave breaking) changes and τ is the typical time scale of a

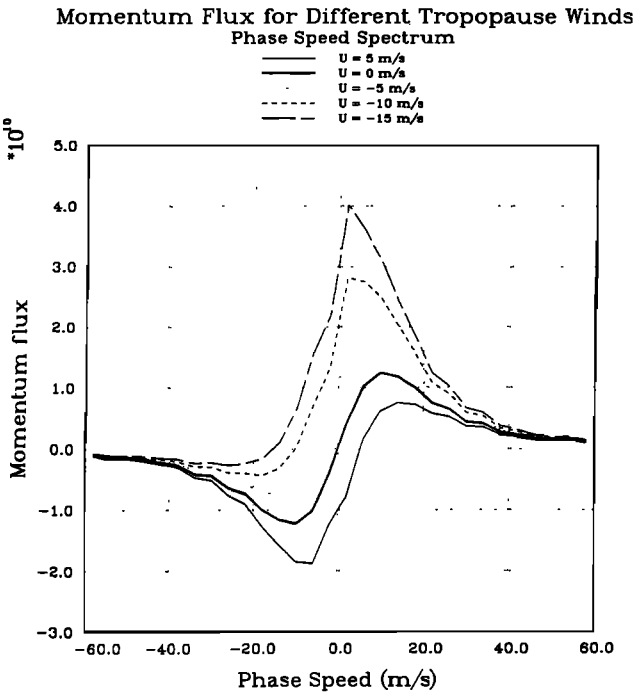

Fig. 22. Time-and area-integrated vertical flux of zonal momentum excited by the disturbance described by (21) with $p_0 = 300$ m, for several tropopause zonal wind speeds.

convectively active period. During STEP, convective periods typically lasted on the order of a week [*Selkirk*, this issue]; significant changes in convective activity occur on a scale of about 30° along a latitude circle. With these values the effective divergence associated with gravity wave breaking in the lower stratosphere above the STEP region is $7.0 \times 10^{-8} s^{-1}$, which is comparable though significantly smaller than that expected from diabatic cooling associated with thick cirrus.

Of course, this scaling argument says nothing about the nature of the cross-isentropic circulation induced by the gravity wave drag in the lower stratosphere: this would require more detailed modeling beyond the scope of this work. Also, unlike diabatic cooling overlying cloud shields, gravity wave drag is only important in regions where a strong easterly jet underlies a region of weaker winds.

6. Summary

The most important result of this paper is that the mesoscale fluctuations in the temperature field found over convective systems are indeed gravity waves. Moreover, the good agreement between the model simulations and the observations in Figure 17 lends credence to the simplified mechanism postulated for their generation, namely, the hypothesis of rising and falling convective "mountains" with spatial scales of ~100 km and time scales of several hours. For the case under study, the system exciting the gravity wave was embedded in a tropical cyclone. In fact, as far as the generation of transient gravity waves is concerned, the cyclone is very similar to the convective anvils examined by *Danielsen* [1982]. In that case, the large, long-lived (half a day) convective systems consisted of many quasi-circular cells of ~100 km scale that grew and decayed with ~ 5-hour lifetimes.

The second important result is the evaluation of a characteristic height amplitude for the convective topography of ~450-600 m. This is important, since the vertical flux of horizontal momentum generated by a convective system, and thus the potential impact on the overlying stratosphere, is proportional to the square of the height amplitude. If this is the characteristic amplitude of mesoscale convection for the global tropics, these large amplitudes imply that mesoscale gravity waves are important not only for the westerly phase of the upper stratospheric SAO but also for the easterly phase of the QBO. These statements are subject to a number of uncertainties in addition to uncertainties in the height amplitude. These are, in order of importance, (1) global cloudiness statistics (see *P1*) and (2) the degree of wave breaking in the lower stratosphere.

Finally, there is some evidence that wave breaking occurs in the lower stratosphere as a result of the weak winds overlying the strong tropopause easterlies. Given the convective gravity wave forcing amplitudes we have calculated and subject to the same uncertainties as those for the middle and upper stratospheric drag, the effect of this lower stratospheric wave breaking on the cross-isentropic circulation may be comparable to that of the above-cloud diabatic cooling.

Acknowledgments. This work was funded by the Atmospheric Chemistry/Process Studies branch of NASA. The authors would like to thank Graeme Stephens and Paul Stackhouse of the Colorado State University for providing the digitized GMS images, the Numerical Aerodynamic Simulation Project at NASA/Ames for providing supercomputing time, and Henry Selkirk of Space Physics Research Institute and Richard Young of NASA/Ames' Space Science Division for helpful comments on the manuscript.

References

Ackerman, T. P., K. N. Liou, F. P. J. Valero, and L. Pfister, Heating rates in tropical anvils, *J. Atmos. Sci., 45*, 1606-1623, 1988.

Chan, K. R., S. G. Scott, T. P. Bui, S. Bowen, and J. Day, Temperature and horizontal wind measurements on the ER-2 aircraft during the 1987 Airborne Antarctic Ozone Experiment, *J. Geophys. Res., 94*, 11,573-11,587, 1989.

Clark, T. L., T. Hauf, and J. P. Kuettner, Convectively forced internal gravity waves: Results from Two-Dimensional Numerical Experiments, *Quart. J. Roy. Meteor. Soc., 112*, 899-925, 1986.

Coy, L., Kelvin wave packets and flow acceleration: A comparison of modeling and observations, *J. Atmos. Sci., 41*, 1875-1880, 1984.

Danielsen, E. F., Statistics of cold cumulonimbus anvils based on enhanced infrared photographs, *Geophys. Res. Lett., 9*, 601-604, 1982.

Danielsen, E. F., In situ evidence of rapid, vertical, irreversible transport of lower tropospheric air into the lower tropical stratosphere by convective cloud turrets and by larger-scale upwelling in tropical cyclones, *J. Geophys. Res.*, this issue.

Fovell, R., D. Durran, and J. R. Holton, Numerical simulations of convectively generated stratospheric gravity waves. *J. Atmos. Sci., 49*, 1427-1442, 1992.

Fritts, D. C., Gravity wave saturation in the middle atmosphere: A review of theory and observations, *Rev. Geophys. Space Phys., 22*, 275-308, 1984.

Gary, B., Observational results using the microwave temperature profiler during the Airborne Antarctic Ozone Experiment, *J. Geophys. Res., 94*, 11,223-11,232, 1989.

Hamilton, K., and J. D. Mahlman, General circulation model simulation of the semiannual oscillation of the tropical middle atmosphere, *J. Atmos. Sci., 45*, 3212-3235, 1988.

Heymsfield, G. M., and R. H. Blackmer, Satellite-observed characteristics of midwest severe thunderstorm anvils, *Mon. Weather Rev., 116*, 2200-2224, 1988.

Hitchman, M. H., and C. B. Leovy, Estimation of the Kelvin wave contribution to the semiannual oscillation, *J. Atmos. Sci., 45*, 1462-1475, 1988.

Holton, J. R., The dynamic meteorology of the stratosphere and mesosphere, Meteorol. Monogr., *15*, 216 pp., 1975.

Holton, J. R., *An Introduction to Dynamic Meteorology*, 391 pp., Academic, San Diego, Calif., 1979.

Johnson, R. H., W. A. Gallus, Jr., and M. D. Vescio, Near-tropopause

vertical motion within the trailing region of a midlatitude squall line, *J. Atmos. Sci., 47*, 2200-2210, 1990.

Kelly, K., M. Proffitt, K. R. Chan, M. Loewenstein, J. R. Podolske, S. E. Strahan, J. C. Wilson, and D. Kley, Water vapor and cloud water measurements over Darwin during the STEP 1987 tropical mission, *J. Geophys. Res.*, this issue.

Knollenberg, R. G., K. Kelly, and J. C. Wilson, Measurements of high number densities of ice crystals in the tops of tropical cumulonimbus, *J. Geophys. Res.*, this issue.

Miyahara, S., Y. Hayashi, and J. D. Mahlman, Interactions between gravity waves and planetary-scale flow simulated by the GFDL "SKYHI" general circulation model, *J. Atmos. Sci., 43*, 1844-1861, 1986.

Newell, R. E., and S. Gould-Stewart, A stratospheric fountain?, *J. Atmos. Sci., 38*, 2789-2796, 1981.

Pfister, L., W. Starr, R. Craig, M. Loewenstein, and M. Legg, Small-scale motions observed by aircraft in the tropical lower stratosphere: Evidence for mixing and its relationship to large-scale flows, *J. Atmos. Sci., 43*, 3210-3225, 1986.

Pfister, L., S. Scott, M. Loewenstein, S. Bowen, and M. Legg, Mesoscale disturbances in the tropical stratosphere excited by convection: Observations and effects on the stratospheric momentum budget. *J. Atmos. Sci.*, 1993.

Proffitt, M. H., et al., In situ ozone measurements within the 1987 Antarctic ozone hole from a high-altitude ER-2 aircraft, *J. Geophys. Res., 94*, 16,547-16,556, 1989.

Russell, P. B., L. Pfister, and H. B. Selkirk, The tropical experiment of the Stratosphere-Troposphere Exchange Project (STEP): Science objectives, operations, and summary findings, *J. Geophys. Res.*, this issue.

Scott, S. G., T. P. Bui, K. R. Chan, and S. W. Bowen, The meteorological measurement system on the NASA ER-2 aircraft, *J. Atmos. Oceanic. Technol., 7*, 525-540, 1990.

Selkirk, H. B., The tropopause cold trap in the Australian monsoon during STEP/AMEX 1987, *J. Geophys. Res.*, this issue.

Smith, R. B., Linear theory of stratified hydrostatic flow past an isolated mountain, *Tellus, 32*, 348-364, 1980.

Starr, W. L., and J. F. Vedder, Measurements of ozone in the Antarctic atmosphere during August and September 1987, *J. Geophys. Res., 94*, 11,449-11,464, 1989.

T. P. Bui, K. R. Chan, and L. Pfister, NASA/Ames Research Center, Mail Stop 245-5, Moffett Field, CA 94035-1000.

S. Bowen, San Jose State University, 1 Washington Sq., San Jose, CA 95192.

B. Gary, MS T1182, Jet Propulsion Laboratory, 4800 Oak Grove Drive, Pasadena, CA 91109.

K. Kelly and M. Proffitt, NOAA Aeronomy Laboratory, 325 Broadway, Boulder, CO 80303.

M. Legg, Synernet, 3155 Kearney Street, Suite 170, Fremont, CA 94538.

W. Starr, 13124 Byrd Lane, Los Altos Hills, CA 94022.

(Received March 19, 1992;
revised July 7, 1992;
accepted July 10, 1992.)